DEVELOPING OPTIMAL MASS MATRICES FOR MEMBRANE TRIANGLES WITH CORNER DRILLING FREEDOMS

by

Qiong Guo

B.S. Harbin Institute of Technology, 2008

M.S. Harbin Institute of Technology, 2010

A thesis submitted to the

Faculty of the Graduate School of the

University of Colorado in partial fulfillment

of the requirement for the degree of

Master of Science

Department of Aerospace Engineering Sciences

2012

This thesis entitled:
Developing optimal mass matrices for membrane triangles
with corner drilling freedoms
written by Qiong Guo
has been approved for the Department of Aerospace Engineering Sciences

Carlos Felippa

H. Jerry Qi

Date

The final copy of this thesis has been examined by the signatories, and we
find that both the content and the form meet acceptable presentation standards
of scholarly work in the above mentioned discipline.

Qiong Guo (M.S., Department of Aerospace Engineering Sciences)

Developing optimal mass matrices for membrane triangles with corner drilling freedoms

Thesis directed by Professor Carlos Felippa

This thesis studies the construction of improved mass matrices for dynamic structural analysis using the finite element method (FEM) for spatial discretization. Two kinetic-energy discretization methods described in FEM textbooks since the mid-1960s lead to diagonally-lumped and consistent mass matrices, respectively. While these well-known models are sufficient to cover many engineering applications, they may fail to satisfy customized optimality conditions, such as delivering better accuracy in the low frequency (long wavelength) limit, which is important in structural dynamics and vibrations. Such gaps can be filled with a more general approach that relies on the use of mass templates. These are algebraic forms that carry free parameters. Templates have the virtue of producing a set of mass matrices that satisfy certain a *priori* constraint conditions such as symmetry, nonnegativity, observer invariance and linear momentum conservation. In particular, the diagonally-lumped and consistent mass versions can be obtained as instances; thus those standard models are not excluded. The presence of free parameters, however, allows the mass matrix to be customized to specific needs. A mass template is called optimal if it meets a quantifiable “best” criteria, such as highest low-frequency accuracy, for certain values of the parameters.

The present work develops such conditions by studying the propagation of two types of plane waves: P (pressure) and S (shear), over regular, infinite, square-cell FEM lattices of isotropic plates. Such studies are equivalent to directional Fourier analysis. Only one-parameter templates, obtained by linear weighting lumped and quasi-consistent mass matrix instances, are considered. Using a computer algebra system (CAS), exact dispersion expressions are obtained for the two elements under study. In addition to the free parameter, dispersion is found to depend on three factors: Poisson's ratio, propagation angle with respect to lattice principal directions, and wave type (P or S). Exact expressions are Taylor expanded in the low frequency limit and matched, using the template parameter, with the continuum dispersion up to maximum possible order in the wavenumber. Matches are further averaged over propagation angle and Poisson's ratio ranges to provide recommended values for use in existing FEM codes.

The present work represents the first work of this nature for two-dimensional finite elements. It was made possible by steady improvements in CAS software, as well as CPU and RAM computer resources. As summarized in the Conclusions Chapter, these initial results suggest future-work extensions that remove several of the simplifying assumptions made in this study.

DEDICATION

I would like to dedicate this work to my parents and my husband for their continual love and support without which this thesis would not be possible.

ACKNOWLEDGMENTS

Above all, I would like to thank my advisor, Prof. Carlos Felippa, for his invaluable support of this work. I appreciate his patience and guidance.

I express my thanks to the rest of my committee members: Prof. H. Jerry Qi, Prof. Alireza Doostan for their advice.

I would also like to thank all of my past colleagues for their assistances and entertainment in life.

I am grateful to the Center for Aerospace Structures for providing support for the research work reported here.

CONTENTS

LIST OF TABLES

Table

LIST OF FIGURES

Figure

CHAPTER 1

INTRODUCTION

1.1 Project Motivation and Literature Review

1.1.1 High-performance Elements

The development of high-performance (HP) elements has been an active area of finite element technology since the early 1980s. The "high performance" qualification of such elements depends on subjective evaluation criteria. A result-oriented definition given in [1] characterizes them as : "simple elements that provide results of engineering accuracy with coarse meshes". This is agreement with the experience of engineering users of the method.

What is the definition of simple elements? Following the high-order element development frenzy of the late 1960s and 1970s, the trend back towards simplicity was noted as early as 1986 by R. H. MacNeal, who is well known as the FEM community as the father of NASTRAN: "The limitations of higher order elements set out by Zienkiewicz have proved themselves in application. As a practical matter, the real choice is between lowest order elements (constant strain, probably with some linear strain terms) and next-lowest-order elements (linear strain, possibly with some quadratic strain terms), because these are the ones that developers of finite element programs have found to be commercially viable"[2]. From this quote we can conclude that elements with only corner nodes and physical degrees of

freedom can qualify as simple elements. The trend of using simple elements has strengthened since that statement. As commercial FEM codes are now widely used in industry, most of their users have only a dim idea of what goes on inside those "black boxes". Thus the attraction of HP elements in the engineering world is understandable: to get reasonable answers with models that cannot stray too far from physics.

There are generally three element derivation approaches for constructing HP elements, as summarized in [3]. They are fixing up, retrofitting and direct fabrication. Among them direct fabrication appears to be most effective for creating HP elements. The element equation components, such as the stiffness and mass matrices, may contain *free parameters*. These may be used to improve performance and eventually to try for optimality while keeping the element configuration in terms of both geometry and degrees of freedom fixed. A general scheme for direct fabrication is the *template* approach.

1.1.2 Drilling Freedoms

One side effect of the growing interest in HP elements is the proliferation of elements with drilling degrees of freedom (DOFs). Drilling freedoms are nodal rotations that in conventional elements are not independent DOFs. By contrast, in this thesis we consider corner rotations normal to the plane of a membrane element (or to the membrane component of a shell element) as independent DOF. Motivations for including drilling freedoms include the following, listed in [4]:

1. The element performance may be improved without adding midside nodes, keeping model preparation and mesh generation simple.

2. When used for the membrane component of shell elements, the extra degree of freedom is "free of charge" in programs that carry six DOFs per node, as is the case in most commercial codes.

3. It simplifies the treatment of shell intersections as well as connection of shells to beam elements, such as those modeling edge stiffeners.

Many efforts were made during the period 1964-1975 to develop membrane elements with drilling freedoms without success. This early work is summarized in the Introduction of [5]. The first successful membrane triangles with drilling freedoms were presented by Allman in 1984 [6] and Bergan and Felippa in 1985 [5]. The two approaches share procedural similarities, such as the use of incompatible displacement functions, and can be extended to quadrilateral elements with drilling freedoms for plane stress and shell analysis. But the element construction methods are totally different.

Allman used the conventional total potential energy (TPE) formulation. His original element suffered from rank deficiency. This problem was corrected in an improved version published in 1988 [7]. Frey and coworkers in [8] extended this approach to quadrilateral shell elements. A free formulation (FF) based quadrilateral element was constructed by Nygard in his thesis [9] using quadratic and cubic higher order functions.

The approach followed in [5] used the FF presented by Bergan and Nygard [10] in 1984. For the definition of drilling DOF they exploited the concept of continuum-mechanics rotations, following mid-1960s work at Berkeley [11-13]. The element constructed in 1984 lacked a variational basis. This deficiency was remedied five years later by the introduction of parametrized variational principles in a series of publications [14-16]. A full discussion of the formulation of 3-node, 9-dof membrane elements with drilling freedoms and the performance of these elements are given in a three-Part series [4, 17, 18]. After that Felippa [3] constructed an optimal three-node, 9-dof membrane triangles stiffness matrix based on *templates* [19, 20]. These are algebraic forms that carry free parameters. By using templates it is possible to search for optimal or customize element instances. They are also useful in research studies because a template spans an infinity of possible elements. These may include already published elements, as well as new ones. The element derived in [3] is "optimal" in the sense of achieving exact inplane pure-bending response of rectangular mesh units of arbitrary aspect ratio. The template approach was further developed by Haugen in his 1994 thesis [21] to construct triangular and quadrilateral shell elements with drilling rotations, which were used for nonlinear shell analysis.

1.1.3 Lumped and Consistent Mass Matrices

To carry out dynamic finite element analysis (an application that embodies vibrations and wave propagation), we need a mass matrix to pair with the stiffness matrix. It was shown by Archer [22] that errors in mass modeling may cause sizable

errors in the natural frequencies, which in turn impairs the accuracy of the dynamic response. Thus it is of great interest to construct "HP mass matrices" that can be paired to a HP stiffness matrix. The underlying idea is to keep the same element geometry DOF configuration but to adjust the mass matrix to achieve optimal behavior in some sense.

As a general rule, the construction of the master mass matrix **M** largely parallels that of the master stiffness matrix **K**. Mass matrices for individual elements are formed in local coordinates, transformed to the global frame, and merged into the master mass matrix following exactly the same techniques used for **K**. In practical terms, the assemblers for **K** and **M** can be made identical. This procedural uniformity is one of the great assets of the Direct Stiffness Method. Consequently, in this study we can focus attention on the construction of the mass matrix for an *individual element*.

The element mass matrix follows from a consistent derivation from the variational formulation, using the same shape function as in the derivation of the stiffness matrix, is called *consistent mass matrix* (CMM). The CMM is generally full at the element level because the shape functions are usually coupled. When assembled, the master CMM has a sparseness similar to that of the master stiffness matrix. Use of this matrix is known to overestimate natural frequencies, especially for higher modes.

As an alternative, a diagonal mass matrix based on direct lumping to the nodal DOF is often used. This has the benefit of providing a diagonal master mass

matrix, which is easily inverted. The resulting computational savings are especially important in explicit time integration. In addition, some second-order [23] and third-order [24] accurate implicit methods depend on diagonal mass. The use of a diagonal mass has also been shown useful in reducing numerical dispersion in wave propagation problems [25, 26]. Thus the effective diagonalization of the consistent mass matrix has been a topic of research, mainly focusing on minimizing the loss of accuracy as a result of compressing information. A mass matrix constructed in this way is called *diagonally lumped mass matrix* (DLMM).

The simplest mass lumping approach divides the total mass among the diagonal entries of the consistent mass matrix while setting all other off-diagonal entries to zero. A more refined diagonalization scheme replace the diagonal entries by the MCC row sums [27].

A widely cited article on mass lumping schemes was written by Hinton, Rock and Zienkiewicz [28] in 1976. Starting from a fully coupled CMM, they recommend to lump by ignoring the off-diagonal entries and scaling the diagonal entries through an appropriate factor that preserves the total translational mass of the element. The procedure is now called the HRZ diagonalization method. It is rated by Cook, Malkus and Plesha [29] as an effective lumping method for arbitrary elements. In fact the HRZ agonalization is not always optimal for high order elements as proved by Malkus and Plesha [30]. For such elements in multiple dimensions, optimal mass lumping schemes may lead to zero and negative masses.. This approach may cause, however, spurious dynamic stability problems in direct

time integration. Results are presented in [31] for both vibration and dynamics analysis, and for unstable transient finite element analysis in [32]. Another so-called “optimal lumping” [33] is obtained by evaluating the finite element mass matrix using a Lobatto numerical integration scheme in which the integration points coincide with the element nodes.

The mass lumping methods mentioned above only consider the translational mass lumped to the nodes. For elements with both translational and rotational degrees of freedom, such as beams and plates, mass terms associated with the rotational DOF are often ignored by setting the corresponding diagonal terms to zero. That may result in accuracy cost. To increase accuracy, Archer and Whalen [34] developed a new diagonalization technique for a rotationally consistent diagonal mass matrix, called the RC method. It is achieved by scaling nonzero diagonal rotational mass terms such that the total rotational inertia between the original consistent and new diagonal mass matrix agree. A comparison between lumped, HRZ and RC diagonalization methods for beam and plate elements was also presented in that article.

In dynamic contact problems, numerical stability may be significantly improved via modification of the mass matrix [35, 36]. Tkachuk [37] constructed a singular hybrid-mixed mass matrix for both bulk and thin-walled structures through special selection of the trial space and displacement shape functions. It allows entries of the mass matrix to vanish at specific nodes, while the mass is redistributed at the element level from the corner nodes to mid-side and inner

nodes. Only the corner nodes are used later for contact collocation. The new elements show superior results for such applications, especially by reducing artificial oscillations of contact pressures as well as achieving exact energy preservation.

The above reviewed work suggests that while conventional approaches to mass matrix construction are by now well developed, further improvements are possible. For example, CMM and DLMM are known to overestimate and underestimate, respectively, continuum natural frequencies. This suggests that a weighted contribution of the two might improve accuracy. Such a combination is explored here using the template approach. For 2D elements, this is the first such study.

1.2 Scope of Research

An optimal element is, loosely speaking, one whose performance cannot be improved for a given node-freedom configuration. However, such an element may not be necessarily unique, even for the simplest one-dimensional models, unless one specifies precisely the optimality criterion. Such specification depends on simulation needs and objectives.

One customization scenario is *high fidelity systems*. Dynamic analysis covers a wide range of applications. There is a subclass that calls for a level of simulation precision beyond that customary in engineering analysis. Examples are deployment of precision structures, resonance analysis of machinery or equipment, adaptive active control, ultrasonic imaging, signature detection, radiation loss in layered

circuits, and molecular- and crystal-level simulations in micro- and nano-mechanics. In structural static analysis an error of 20% or 30% in peak stresses is not cause for alarm — such discrepancies are usually covered adequately by safety factors. But a similar error in frequency analysis or impedance response of a high fidelity system may be disastrous. Model mesh adaptivity comes to the rescue in statics; but this is less effective in dynamics on account of the time dimension. Achieving acceptable precision with a fine mesh, however, can be expensive. Customized elements may provide a practical solution: achieving adequate accuracy with a coarse regular mesh.

To customize the mass for a specific dynamic problem need, we need a sharper toolset instead of conventional error analysis in FEM, which only gives worst-case asymptotic convergence rates in some norm. This is where “templates” come in. Through adjusting free parameters, the mass template may include all instances from DLMM to CMM, as well as combination of the two. An attractive feature of templates for FEM is that each “custom mass matrix” need not be coded and tested individually. Only a single programming module, to which free parameters are passed as arguments, can take care of all possibilities. However the ability to customize the mass matrix is not free of cost. A significant amount of algebraic work is needed during the element development process, particularly in 2D and 3D. Hand computations rapidly become unfeasible and error prone. Help from a computer algebra system (CAS) is needed to complete the task. *Mathematica*

was used in the present work to carry out the parametrized spectral computations required by template approach.

Template derivations may become exceedingly difficult, even for 1D elements, compared with those based on standard procedures, according to previous research on the bar and plane beam problems [38]. This thesis extends such procedures for the first time to 2D elements. Given time limitations, this work only focuses on getting an improved mass of the plane stress membrane triangle with corner drilling DOF. For expediency, only one template parameter is kept for customization. To find the optimal parameter, a specific optimality criterion is introduced: best match of low frequency dispersion curves with those of the continuum (analytical) model.

One important difference of the 2D (and 3D) problem with respect to 1D is that the FEM mesh introduces directionality dependences over the continuum case [39]. This feature significantly complicates the optimization process.

1.3 Manuscript Organization

The thesis organization is as follows. In Chapter 2 different ways of constructing mass matrices are presented, and the solution method used to find the optimal mass is described. Chapter 3 then describes the details of elements constructed based on the Assumed Natural DEviatoric Strain (ANDES) formulation, which is one variant of the template approach. The lumped mass and quasi-consistent mass matrices are constructed and a mass template containing one free parameter as weighted combination of those. The optimal stiffness matrix for

orthotropic material obtained from [3] is used in the problem, although further derivations are restricted to an isotropic material. For the completeness, the construction of the stiffness template is also covered here. Chapter 4 presents the numerical results of the problem. By comparing the finite element results with the continuum results for low frequency accuracy, the optimal mass matrix is obtained. Finally, Chapter 5 discusses the main results, offers conclusions, and suggests future work on the subject.

CHAPTER 2

MASS MATRIX CONSTRUCTION METHODS

This chapter reviews conventional approaches (direct and variational schemes) to the construction of the mass matrix for a dynamic FEM model. It then focuses on the template approach as generalization.

2.1 Mass Matrix Construction

The master mass matrix is built up from element contributions. Like their stiffness counterparts, mass matrices are often developed in a local frame. Before the merge process, that builds the master mass matrix, a congruent transformation may be required to convert the element mass matrix to the global system.

The construction of the mass matrix of individual elements can be carried out through several methods. These can be categorized into three groups: direct mass lumping, variational mass lumping, and template mass lumping.

2.1.1 Direct Mass Lumping

The total mass of element e is directly apportioned to nodal freedoms, ignoring any cross coupling. The goal is to build a *diagonally lumped mass matrix* or DLMM, denoted here by $\mathbf{M}_L^e$. As a simple example, consider the simplest 1D element: 2-node prismatic bar element with length ℓ, cross section area A, and mass density

ρ, the total mass of the element is $M_T^e = \rho A\ell$, which is divided equally and assigned to the end translational DOF. Hence the diagonally lumped mass matrix is

$$\mathbf{M}_L^e = \frac{1}{2}\rho A\ell \begin{bmatrix} 1 & 0 \\ 0 & 1 \end{bmatrix}. \tag{2.1}$$

This lumping process conserves the translational kinetic energy or, equivalently, the linear momentum. When applied to simple elements that can rotate in 2D or 3D, however, the direct lumping process may not necessarily preserve angular momenta. A key motivation for direct lumping is that, as noted in the Introduction, a diagonal mass matrix may offer significant computational and storage advantages in certain classes of simulation, notably explicit time integration. Furthermore, direct lumping covers naturally the case where concentrated (point) masses are important part of model building. For example, in aircraft engineering it is common to idealize nonstructural masses (fuel, cargo, engines, etc.) as concentrated at given locations. In civil engineering a similar lumping process takes care of nonstructural masses in buildings, such as machinery, insolation and furniture.

The construction of a DLMM is not a unique process, except for very simple elements (such as the 2-node bar illustrated above), in which the lumping is fully defined by conservation and symmetry considerations.

2.1.2 Variational Mass Lumping

A second class of mass matrix construction method is based on a variational formulation. This is done by taking the kinetic energy as part of the governing

functional. The kinetic energy of an element of mass density ρ that occupies the domain e and moves with velocity field $\vec{\mathbf{v}}^e$ is

$$T^e = \frac{1}{2}\int_{\Omega^e} \rho(\vec{\mathbf{v}}^e)^T \vec{\mathbf{v}}^e \, d\Omega^e. \tag{2.2}$$

Following the FEM philosophy, the element velocity field is interpolated by shape functions: $\overrightarrow{\mathbf{v}^e} = \mathbf{N}_v^e \dot{\mathbf{u}}^e$, in which $\dot{\mathbf{u}}^e$ are node DOF velocities and $\mathbf{N}_v^e$ a shape function matrix. Inserting into Eq. (2.2) and moving the node velocities out of the integral gives:

$$T^e = \frac{1}{2}(\dot{\mathbf{u}}^e)^T \int_{\Omega^e} \rho(\mathbf{N}_v^e)^T \mathbf{N}_v^e d\Omega \dot{\mathbf{u}}^e = \frac{1}{2}(\dot{\mathbf{u}}^e)^T \mathbf{M}^e \dot{\mathbf{u}}^e. \tag{2.3}$$

The element mass matrix naturally follows as the Hessian of T^e:

$$\mathbf{M}^e = \frac{\partial^2 T^e}{\partial \dot{\mathbf{u}}^e \partial \dot{\mathbf{u}}^e} = \int_{\Omega^e} \rho(\mathbf{N}_v^e)^T \mathbf{N}_v^e d\Omega. \tag{2.4}$$

If the same shape functions used in the derivation of the stiffness matrix are chosen, that is, $\mathbf{N}_v^e = \mathbf{N}^e$, Eq. (2.4) yields the *consistent mass matrix* or CMM. This instance is denoted here by $\mathbf{M}_C^e$.

2.1.3 Template Mass Lumping

The previous two subsections describe conventional approaches to the construction of the mass matrix. Those lead to CMM and DLMM, respectively. Collectively they take care of many engineering applications in structural dynamics. Occasionally, however, they fall short. The gap can be filled with a more general approach that relies on *templates*. These are algebraic forms that carry free

parameters and represent element-level mass equations. This is the approach we use to construct customized mass matrices in the present work.

The template approach has the virtue of generating a set of mass matrices that satisfy certain *a priori* constraints such as symmetry, nonnegativity, invariance and momentum conservation. In particular, the diagonally-lumped and consistent mass matrices can be obtained as instances. Thus those standard models are not excluded. Availability of free parameters, however, allows the mass matrix to be customized to special needs such as higher accuracy in vibration analysis, or minimally dispersive wave propagation. The set of parameters is called the *template signature*. This signature characterizes uniquely a mass matrix instance.

An attractive feature of templates for FEM programming is that each "custom mass matrix" need not be coded and tested individually. It is sufficient to implement the template as a single element level module, with free parameters as arguments, and simply adjust the signature to the problem at hand. In particular the same module should be able to produce the conventional DLMM and CMM models, which can provide valuable crosschecks.

There are several ways to parametrize mass matrices. Three techniques found effective in practice are summarized below:

Matrix-Weighted Parametrization. A matrix-weighted mass template for element e is a linear combination of $(k + 1)$ component mass matrices, $k \geqslant 1$ of which are weighted by parameters:

$$\mathbf{M}^e = \mathbf{M}_0^e + \mu_1 \mathbf{M}_1^e + \ldots \mu_k \mathbf{M}_k^e, \tag{2.5}$$

Here $\mathbf{M}_0^e$ is the *baseline mass matrix*. This should be an acceptable mass matrix on its own if $\mu_1 = \cdots \mu_k = 0$. The simplest instance of Eq. (2.5) is a linear combination of the consistent and diagonally-lumped mass

$$\mathbf{M}^e = (1-\mu)\mathbf{M}_C^e + \mu\mathbf{M}_L^e, \tag{2.6}$$

This can be reformatted as Eq. (2.6) by writing $\mathbf{M}^e = \mathbf{M}_C^e + \mu(\mathbf{M}_L^e - \mathbf{M}_C^e)$. Here k=1, the baseline is $\mathbf{M}_0^e = \mathbf{M}_C^e$, $\mu \equiv \mu_1$ and $\mathbf{M}_1^e$ is the consistent mass deviator $\mathbf{M}_L^e - \mathbf{M}_C^e$.

Spectral Parametrization. This has the form

$$\mathbf{M}^e = \mathbf{H}^T\mathbf{D}_\mu\mathbf{H}, \quad \mathbf{D}_\mu = \text{diag}\begin{bmatrix} c_0\mu_0 & c_1\mu_1 & \ldots & c_k\mu_k \end{bmatrix}, \tag{2.7}$$

in which $\mathbf{H}$ is a generally full matrix. Parameters $\mu_0 \ldots \mu_k$ appear as entries of the diagonal matrix $\mathbf{D}_\mu$. Scaling coefficients c_i may be introduced for convenience. Configuration (2.7) occurs naturally when the mass matrix is constructed first in generalized mass-orthogonal coordinates, followed by transformation to physical coordinates via $\mathbf{H}$. This method only works for 1D element.

Entry-Weighted Parametrization. An entry-weighted mass template applies parameters directly to every entry of the mass matrix, except for a *priori* constraints, such as those listed below. This form is the most general one and can be expected to lead to the best possible solutions. But it is restricted to simple (usually 1D) elements because the number of free parameters grows quadratically in the matrix size, whereas for the other two schemes it grows linearly.

Combined Approach. A hierarchical combination of parametrization schemes can be used to advantage if the kinetic energy can be naturally decomposed from physics. This combination was used to advantage for the Timoshenko beam

element [38], in which components of a two-matrix-weighted template like (2.4) were constructed by spectral and entry-weighted parametrization, respectively.

2.1.4 Mass Matrix Properties

Mass matrices must satisfy certain conditions that can be used for verification and debugging. They are: (1) matrix symmetry, (2) physical symmetries, (3) conservation and (4) positivity.

Matrix Symmetry. This means $(\mathbf{M}^e)^T = \mathbf{M}^e$, which is easy to check. For a variationally derived mass matrix this follows directly from the definition of Eq. (2.4). For a DLMM it holds automatically, because a diagonal matrix is symmetric.

Physical Symmetries. Element symmetries must be reflected in the mass matrix. For example, the CMM or DLMM of a 2-node prismatic bar element must be symmetric about the antidiagonal: $M_{11} = M_{22}$. To see this, flip the end nodes: the element remains the same and so should the mass matrix.

Conservation. At a minimum, total element mass must be preserved. This is easily verified by applying a uniform translational velocity and checking that linear momentum is conserved. Higher order conditions, such as conservation of angular momentum, are optional, and as previously noted not always desirable.

Positivity. $\mathbf{M}^e$ must be nonnegative. Unlike the previous three conditions, this constraint is nonlinear in the mass matrix entries. It can be tested in two ways: through the eigenvalues of $\mathbf{M}^e$, or by checking the sequence of principal minors. The second technique is more practical if the entries of $\mathbf{M}^e$ are symbolic, unless the matrix order is very small.

2.2 Determination of Template Parameters

After obtaining the DLMM and CMM, we can construct a mass template which contains free parameters. In order to get an optimal signature, i.e., specific numeric values for the free parameters, an optimality criterion must be introduced. Generally the optimal matrix for a certain element is not unique. This indeterminacy may be used to achieve various performance goals by selecting appropriate optimality conditions. This is where customization comes in. For our problem, a useful optimization criterion is the fidelity with which plane waves are propagated over a membrane infinite lattice, when compared to the case of an infinite, continuum thin plate in plane stress. Matching the continuum behavior at all wavelengths is of course impossible because of the FEM discretization. However, a best match to long wavelengths is feasible. This is of interest for structural dynamics applications, in which low frequency behavior dominates.

2.2.1 Plane Wave Propagation

We consider the propagation of a membrane (inplane) harmonic wave that propagates in the x direction in an infinite thin plate. Two types of plane waves occur in 2D/3D infinite media. One is the primary wave, or pressure wave (abbreviation: P-wave), which has the highest velocity. The mode of propagation of a P-wave is always longitudinal; thus, the particles in the solid have vibrations along or parallel to the travel direction of the wave energy. The other is the secondary wave, or shear wave (abbreviation: S-wave), which travels more slowly than the P-

wave. The S-wave moves as a transverse wave, whose motion is perpendicular to the direction of wave propagation.

Symbols used for propagation of harmonic waves in a 2D thin plate are collected in Table 1 for the reader's convenience. A 2D harmonic wave of amplitude B_x and B_y along the x and y axis respectively, is described by the function

$$u_x(x,t) = B_x \exp[i(\mathrm{k}\, x - wt)], \quad u_y(x,t) = B_y \exp[i(\mathrm{k}\, x - wt)], \tag{2.8}$$

in which $i = \sqrt{-1}$. A curve that relates solutions $\omega = \omega(k)$ of Eq. (2.8) is called a *dispersion* relation. For a P-wave, $B_x = B$, and $B_y = 0$. For an S-wave, $B_x = 0$, and $B_y = B$. Consequently Eq. (2.8) can be specialized to both wave types. In addition, the infinitesimal rotation about z axis associated with Eq. (2.8) is

$$\theta_z(x,t) = \frac{1}{2}\left(\frac{\partial u_y}{\partial x} - \frac{\partial u_x}{\partial y}\right) = \frac{1}{2} kiB_y \exp[i(kx - \omega t)]. \tag{2.9}$$

Note that for the P-wave, $\theta_z = 0$ everywhere; thus Eq. (2.9) only occurs for an S-wave.

Table 1. Nomenclature for Harmonic In PlaneWave Propagation in 2D Thin Plate

Quantity	*Meaning* (physical dimension in brackets)
ρ, E, A	Mass density, elastic modulus, and cross section area
$u_x(x,t)$	Waveform in x-direction $u_x = B_x \exp(i(k_x x - \omega t))$ [length]
$u_y(x,t)$	Waveform in y-direction $u_y = B_y \exp(i(k_y x - \omega t))$ [length]
B	Wave amplitude [length]
λ	Wavelength [length]

k	Wavenumber $k = 2\pi/\lambda$ [1/length]
ω	Circular (angular) frequency $\omega = kc = 2\pi f = 2\pi c/\lambda$ [radians/time]
f	Cyclic frequency $f = \omega/2\pi$ [Hz]
T	Period $T = 1/f = 2\pi/\omega = \lambda/c$ [time]
c	Phase velocity $c = \omega/k = \lambda/T = \sqrt{E/\rho}$
χ	Element-to-wavelength ratio $\chi = \ell/\lambda$
κ	Dimensionless wavenumber $\kappa = k\lambda$
Ω	Dimensionless circular frequency $\Omega = \omega T = \omega\lambda/c$

2.2.2 Fourier Analysis

To obtain the dispersion curve for a FEM-discretized infinite plate lattice we resort to Fourier analysis to separate space and time. The same procedure applies to both wave types. The lattice propagation process is governed by the linear, unforced, semidiscrete, dynamical equations of motion (EOM)

$$\mathbf{M}\ddot{\mathbf{u}} + \mathbf{K}\mathbf{u} = \mathbf{0}, \tag{2.10}$$

in which a superposed dot denotes differentiation with respect to time t. Eq. (2.10) can be solved by standard Fourier methods. The operational techniques introduced by Park and Flaggs [40, 41] for finite element analysis are used. To study solutions it is sufficient to extract a typical seven-node patch as that illustrated in Figure 1. The lattice patch consists of six triangles surrounding a center point, with nodes ordered counter clockwise around the origin. Only triangles with one 90° angle are considered for simplicity. The finite element lengths in x and y direction are identical: $L_{ex} = L_{ey}$.The patch is swept by P-waves and S-waves of varying frequency

and wavenumber. Both plane waves are assumed to propagate along the x axis. Eq. (2.10) over the patch becomes

$$\mathbf{M}_p\ddot{\mathbf{u}}_p + \mathbf{K}_p\mathbf{u}_p = \mathbf{0}, \tag{2.11}$$

where $\mathbf{M}_p$ and $\mathbf{K}_p$ are the 21×21 assembled master mass matrix and master stiffness matrix of the patch, respectively, and $\mathbf{u}_p$ is a 21×1 DOF patch vector. Eq. (2.11) is equivalent to Eq. (2.12)

$$(\mathbf{K}_p - \omega^2\mathbf{M}_p)\mathbf{u}_p = \mathbf{0}. \tag{2.12}$$

A known stiffness matrix and the mass template to be investigated and plugged into the patch equation (2.12). Usually the stiffness is that of an optimal template instance. From the patch equation formed we extract the first three equations, which correspond to the three DOFs retaining to node 1. This extraction process is justified if the patch *repeats* into the infinite lattice, as this assumption permits the use of periodic conditions. Contracting the first three equations of $(\mathbf{K}_p - \omega^2\mathbf{M}_p)$ with $\mathbf{u}_p$ gives 3 homogeneous equations, from which a time-dependent harmonic factor (the complex exponential in Eqs. (2.8)-(2.9)) can be separated. The remaining factor is required to have nontrivial solutions, that is

$$B_x \neq 0 \text{ for P-wave,} \quad \text{or } B_y \neq 0 \text{ for S-wave.} \tag{2.13}$$

Condition (2.13) leads to three *residual equilibrium equations* which collectively produce an *eigenvalue* problem in ω^2, which sorted as

$$\omega^2 = \omega^2(k). \tag{2.14}$$

which produces the dispersion curve of the FEM lattice. The low-frequency behavior, which as noted is used for optimization, is obtained by Taylor series of Eq.

(2.14) about $k = 0$ for positive wavenumbers k. Comparison with the continuum dispersion provides the optimal parameter.

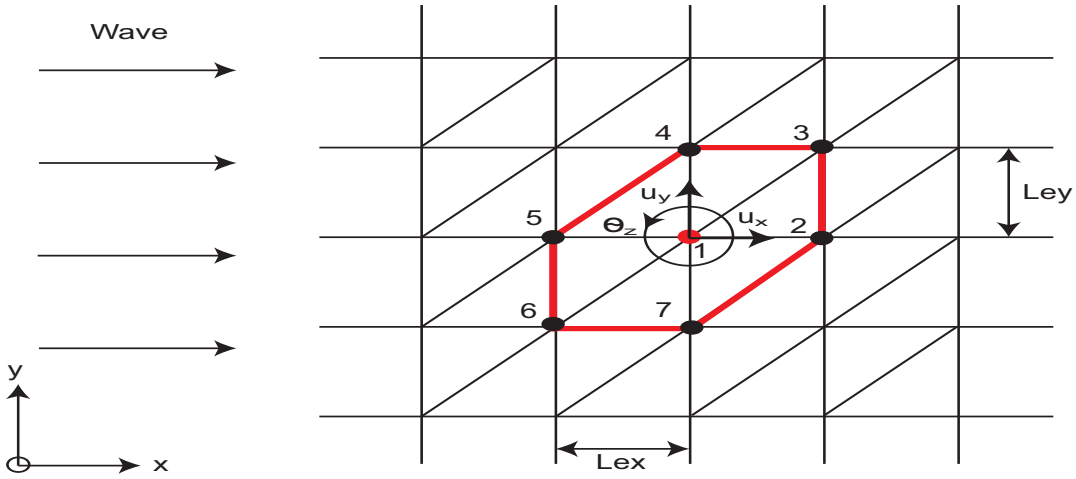

Figure 1. Illustration of patch

CHAPTER 3

TRIANGULAR MEMBRANE ELEMENTS

This chapter presents the geometry and degree-of-freedom (DOF) configuration of two instances of triangular membrane elements: a six-node triangle and a 3-node triangle with drilling DOF. These instances have 12 and 9 DOF, respectively. Geometric and constitutive (material) properties are described, along with behavioral assumptions required for element derivation.

3.1 Element Geometry

As pictured in Figure 2 (b), the membrane linear strain triangle considered here has three corner nodes and three DOFs per node: two inplane translations and a drilling rotation. It is identified by the acronym LST-3/9R. Its parent element is the conventional linear strain triangle, which is technically identified by the acronym LST-6/12C. This triangle has six nodes and two DOFs per node: two inplane translations, shown in Figure 2 (a). The parent element is the most general type of element with quadratic polynomial shape function. Simply by reconfiguration of DOFs, it can produce its descendants. In this case, the LST-3/9R element is obtained from the LST-6/12R element by deleting 3 DOFs (total: 12 to 9 DOFs) and moving 3DOFs to the corner nodes.

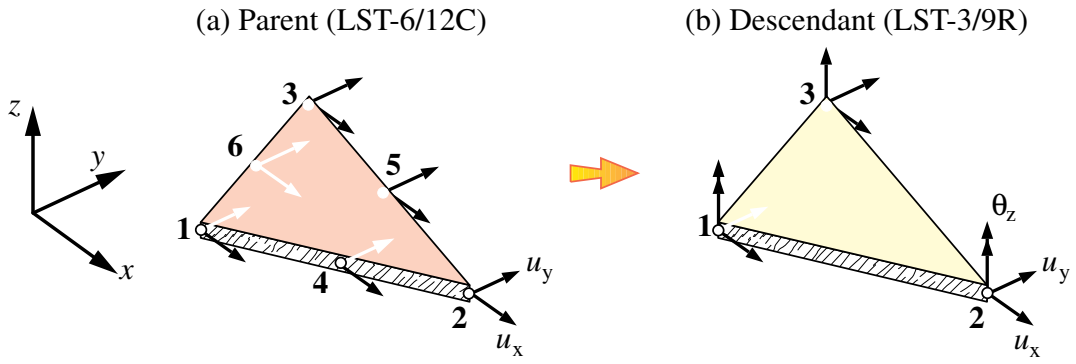

Figure 2. Node and DOF configurations of the linear-strain membrane triangles: (a) the "parent" LST-6/12C (b) its descendant LST-3/9R.

Both membrane (plane stress) triangles shown in Figure 2 (a, b) has straight sides. Its geometry is completely defined by the coordinates of its three corner nodes $\{x_i, y_i\}$, $i = 1, 2, 3$, with respect to a Cartesian coordinate system (x, y). Coordinate differences are abbreviated $x_{ij} = x_i - x_j$ and $y_{ij} = y_i - y_j$. The element is referred to a local Cartesian system (x, y). The Cartesian distances from the nodes to the triangle centroid $x_0 = (x_1 + x_2 + x_3)/3$, $y_0 = (y_1 + y_2 + y_3)/3$ are denoted by $x_{i0} = x_i - x_0$ and $y_{i0} = y_i - y_0$. It follows that

$$x_{10} + x_{20} + x_{30} = 0, \quad y_{10} + y_{20} + y_{30} = 0. \tag{3.1}$$

The signed triangle area A is given by the formula

$$2A = (x_2 y_3 - x_3 y_2) + (x_3 y_1 - x_1 y_3) + (x_1 y_2 - x_2 y_1) = (y_{21} x_{13} - x_{21} y_{13}). \tag{3.2}$$

The corner nodal numbering (1->2->3) is chosen so that $A > 0$. To streamline derivation we also make use of dimensionless triangular coordinates (also known as area coordinates in the FEM literature) $(\zeta_1, \zeta_2, \zeta_3)$, which are linked by the constraint

$$\zeta_1 + \zeta_2 + \zeta_3 = 1. \tag{3.3}$$

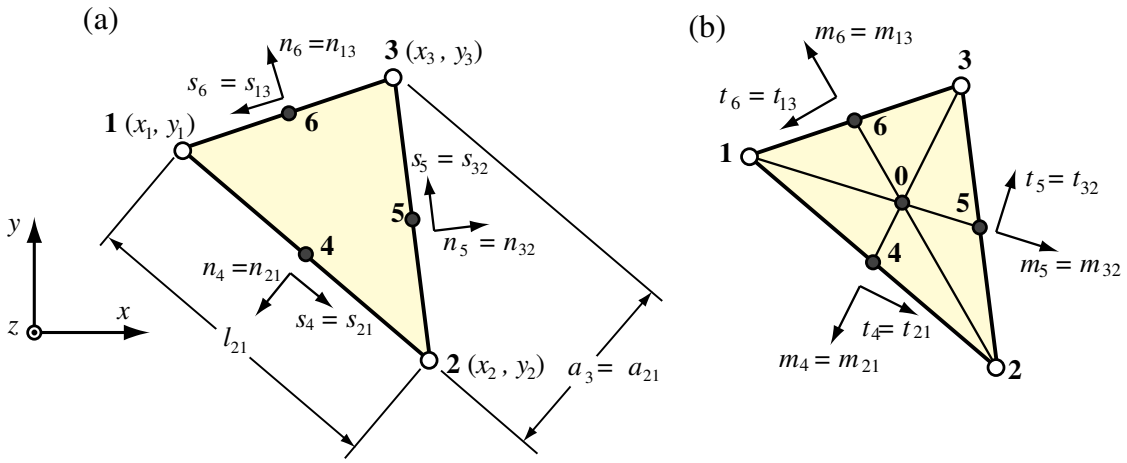

Figure 3. Triangle geometry

Other intrinsic triangle dimensions of use in subsequent derivations, shown in Figure 3, are

$$\begin{aligned} &\ell_{ij} = \ell_{ji} = \sqrt{x_{ij}^2 + y_{ij}^2}, \quad a_{ij} = a_{ji} = \frac{3}{2}\sqrt{x_{k0}^2 + y_{k0}^2}, \quad b_{ij} = 2A / a_{ij}, \\ &S_1 = \frac{1}{4}(\ell_{12}^2 - \ell_{31}^2), \quad S_2 = \frac{1}{4}(\ell_{23}^2 - \ell_{12}^2), \quad S_3 = \frac{1}{4}(\ell_{13}^2 - \ell_{23}^2). \end{aligned} \tag{3.4}$$

in which j and k denote the positive cyclic permutations of i; for example $i = 2, j = 3, k = 1$. Here ℓ_{ij} and a_{ij} denote lengths of the triangles sides and medians, respectively, while b_{ij} are side lengths projected on normal-to-median directions.

In addition to the corner nodes 1, 2 and 3 we shall also use the midpoints 4, 5 and 6 for intermediate derivations, although these nodes do not appear in the final equations of the LST-3/9R element. They are located opposite corners 3, 1 and 2, respectively. As depicted in Figure 3, two intrinsic coordinate systems are used on each triangle side:

$$n_{21}, s_{21}, \quad n_{32}, s_{32}, \quad n_{13}, s_{13}, \tag{3.5}$$

$$m_{21}, t_{21}, \quad m_{32}, t_{32}, \quad m_{13}, t_{13}. \tag{3.6}$$

Here n and s are oriented along the external normal-to-side and side directions, respectively, whereas m and t are oriented along the triangle median and normal-to-median directions, respectively. The coordinate sets (3.5) and (3.6) align only for equilateral triangles. The origin of these systems is left "floating" and may be adjusted as appropriate. If the origin is placed at the midpoints, subscripts 4, 5 and 6 may be used instead of 21, 32 and 13, respectively, as illustrated in Figure 3.

The DOFs of LST-3/9R are collected in the node displacement vector

$$\mathbf{u_R} = \begin{bmatrix} u_{x1} & u_{y1} & \theta_1 & u_{x2} & u_{y2} & \theta_2 & u_{x3} & u_{y3} & \theta_3 \end{bmatrix}. \tag{3.7}$$

Here u_{xi} and u_{yi} denote the nodal values of the translational displacements u_x and $u_y$along x and y, respectively, and $\theta \equiv \theta_z$ are the small "drilling rotations" about z (positive counterclockwise when looking down on the element midplane along -z). In continuum mechanics these infinitesimal rotations are defined by

$$\theta = \theta_z = \frac{1}{2}\left(\frac{\partial u_y}{\partial x} - \frac{\partial u_x}{\partial y}\right). \tag{3.8}$$

3.2 Natural Strains

The derivation of the LST-3/9R stiffness matrix template is based on the Assumed Natural DEviatoric Strain (ANDES) method introduced in [17]. In this method *natural strains* play a key role. These are extensional (direct) strains along three directions intrinsically related to the triangle geometry. Four possible choices

are depicted in Figure 4. Choice #(s): strains along the three side directions, was the one selected in [17] because it matches the direction of neutral axes of assumed inplane bending modes. These modes are important in the derivation of the higher order stiffness template, as described later.

The (s) natural strains are collected in the 3-vector

$$\boldsymbol{\varepsilon} = [\varepsilon_{21} \quad \varepsilon_{32} \quad \varepsilon_{13}]^T. \tag{3.9}$$

Vector $\boldsymbol{\varepsilon}$ evaluated at point i is denoted by $\boldsymbol{\varepsilon_i}$. The natural strains are related to Cartesian strains $\{e_{xx}, e_{yy}, 2e_{xy}\}$ by the transformation

$$\boldsymbol{\varepsilon} = \begin{bmatrix} \varepsilon_{12} \\ \varepsilon_{23} \\ \varepsilon_{31} \end{bmatrix} = \begin{bmatrix} x_{21}^2/\ell_{21}^2 & y_{21}^2/\ell_{21}^2 & x_{21}y_{21}/\ell_{21}^2 \\ x_{32}^2/\ell_{32}^2 & y_{32}^2/\ell_{32}^2 & x_{32}y_{32}/\ell_{32}^2 \\ x_{13}^2/\ell_{13}^2 & y_{13}^2/\ell_{13}^2 & x_{13}y_{13}/\ell_{13}^2 \end{bmatrix} \begin{bmatrix} e_{xx} \\ e_{yy} \\ 2e_{xy} \end{bmatrix} = T_e^{-1} e \tag{3.10}$$

The inverse relation is

$$\begin{bmatrix} e_{xx} \\ e_{yy} \\ 2e_{xy} \end{bmatrix} = \frac{1}{4A^2} \begin{bmatrix} y_{23}y_{13}\ell_{21}^2 & y_{31}y_{21}\ell_{32}^2 & y_{12}y_{32}\ell_{13}^2 \\ x_{23}x_{13}\ell_{21}^2 & x_{31}x_{21}\ell_{32}^2 & x_{12}x_{32}\ell_{13}^2 \\ (y_{23}x_{31}+x_{32}y_{13})\ell_{21}^2 & (y_{31}x_{12}+x_{13}y_{21})\ell_{32}^2 & (y_{12}x_{23}+x_{21}y_{32})\ell_{13}^2 \end{bmatrix} \begin{bmatrix} \varepsilon_{12} \\ \varepsilon_{23} \\ \varepsilon_{31} \end{bmatrix} \tag{3.11}$$

or, in compact matrix notation, $\mathbf{e} = \mathbf{T}_e \boldsymbol{\epsilon}$. Note that $\mathbf{T}_e$ is constant over the triangle, which is a consequence of assuming straight sides. The natural stress-strain matrix $\mathbf{E}_{nat}$ is defined by

$$\mathbf{E}_{nat} = \mathbf{T}_e^{\mathrm{T}} \mathbf{E} \mathbf{T}_e, \tag{3.12}$$

which is also constant over the triangle. $\mathbf{E}$ is the constitutive matrix for stress-strain relation in Cartesian coordinate. This matrix relates natural stresses collected in 3-vectoe $\boldsymbol{\tau}$ by $\boldsymbol{\tau} = \mathbf{E}_{nat}\boldsymbol{\epsilon}$. However, natural stresses are not directly used in the element derivation.

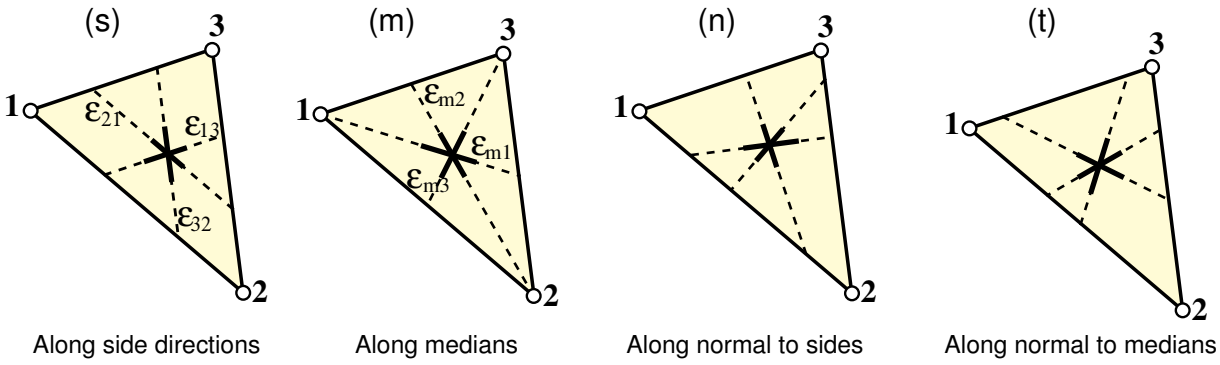

Figure 4. Four choices for natural strains. Labels (s) through (t) correlate with the notation (3.5) and (3.6).

3.3 Hierarchical Rotations

Hierarchical drilling freedoms are useful for compactly expressing the higher order behavior of the element. Their geometric interpretation is shown in Figure 5. The total motion is decomposed into constant strain triangle (CST) motion and Hierarchical motion. Here CST is an acronym for the constant strain triangle.

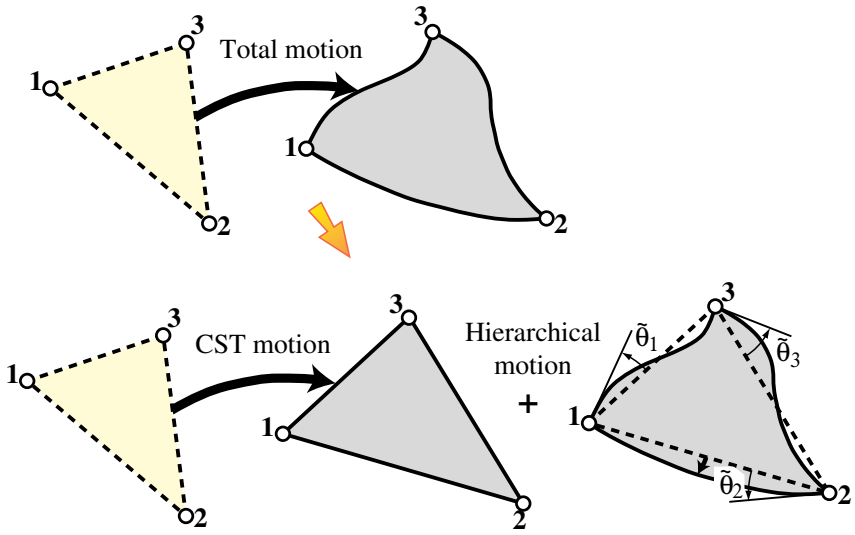

Figure 5. Decomposition of inplane motion into CST (linear displacement) + hierarchical. The same idea (in 2D or 3D) is also important in corotational formulations.

To extract the hierarchical corner rotations $\widetilde{\theta}_i$ from the total corner rotations θ_i, subtract the mean or CST rotation θ_0:

$$\widetilde{\theta}_i = \theta_i - \theta_0, \tag{3.13}$$

where $i = 1, 2, 3$ is the corner index and

$$\theta_0 = \frac{1}{4A}(x_{23}u_{x1} + x_{31}u_{x2} + x_{12}u_{x3} + y_{23}u_{y1} + y_{31}u_{y2} + y_{12}u_{y3}). \tag{3.14}$$

Applying Eqs. (3.13) and (3.14) to the three corners we assemble the transformation that provides hierarchical rotations in terms of the nine DOF:

$$\tilde{\theta} = \begin{bmatrix} \tilde{\theta}_1 \\ \tilde{\theta}_2 \\ \tilde{\theta}_3 \end{bmatrix} = \frac{1}{4A} \begin{bmatrix} x_{32} & y_{32} & 4A & x_{13} & y_{13} & 0 & x_{21} & y_{21} & 0 \\ x_{32} & y_{32} & 0 & x_{13} & y_{13} & 4A & x_{21} & y_{21} & 0 \\ x_{32} & y_{32} & 0 & x_{13} & y_{13} & 0 & x_{21} & y_{21} & 4A \end{bmatrix} \begin{bmatrix} u_{x1} \\ u_{y1} \\ \theta_1 \\ u_{x2} \\ u_{y2} \\ \theta_2 \\ u_{x3} \\ u_{y3} \\ \theta_3 \end{bmatrix} = \tilde{\mathbf{T}}_{\theta u} \mathbf{u}_{\mathbf{R}}. \quad (3.15)$$

For some developments it is useful to complete this transformation with the identity matrix for the translational freedoms:

$$\tilde{\mathbf{u}}_{\mathbf{R}} = \begin{bmatrix} u_{x1} \\ u_{y1} \\ \tilde{\theta}_1 \\ u_{x2} \\ u_{y2} \\ \tilde{\theta}_2 \\ u_{x3} \\ u_{y3} \\ \tilde{\theta}_3 \end{bmatrix} = \begin{bmatrix} 1 & 0 & 0 & 0 & 0 & 0 & 0 & 0 & 0 \\ 0 & 1 & 0 & 0 & 0 & 0 & 0 & 0 & 0 \\ \frac{x_{32}}{4A} & \frac{y_{32}}{4A} & 1 & \frac{x_{13}}{4A} & \frac{y_{13}}{4A} & 0 & \frac{x_{21}}{4A} & \frac{y_{21}}{4A} & 0 \\ 0 & 0 & 0 & 1 & 0 & 0 & 0 & 0 & 0 \\ 0 & 0 & 0 & 0 & 1 & 0 & 0 & 0 & 0 \\ \frac{x_{32}}{4A} & \frac{y_{32}}{4A} & 0 & \frac{x_{13}}{4A} & \frac{y_{13}}{4A} & 1 & \frac{x_{21}}{4A} & \frac{y_{21}}{4A} & 0 \\ 0 & 0 & 0 & 0 & 0 & 0 & 1 & 0 & 0 \\ 0 & 0 & 0 & 0 & 0 & 0 & 0 & 1 & 0 \\ \frac{x_{32}}{4A} & \frac{y_{32}}{4A} & 0 & \frac{x_{13}}{4A} & \frac{y_{13}}{4A} & 0 & \frac{x_{21}}{4A} & \frac{y_{21}}{4A} & 1 \end{bmatrix} \begin{bmatrix} u_{x1} \\ u_{y1} \\ \theta_1 \\ u_{x2} \\ u_{y2} \\ \theta_2 \\ u_{x3} \\ u_{y3} \\ \theta_3 \end{bmatrix} = \tilde{\mathbf{T}}_{\mathrm{R}} \mathbf{u}_{\mathbf{R}}. \quad (3.16)$$

The foregoing transformation matrices are constant over the element.

To simplify the problem of building higher order strain fields, we further split the hierarchical rotations into mean and deviatoric:

$$\begin{bmatrix} \tilde{\theta}_1 \\ \tilde{\theta}_2 \\ \tilde{\theta}_3 \end{bmatrix} = \begin{bmatrix} \overline{\theta} \\ \overline{\theta} \\ \overline{\theta} \end{bmatrix} + \begin{bmatrix} \theta_1' \\ \theta_2' \\ \theta_3' \end{bmatrix}, \quad (3.17)$$

in which $\bar{\theta} = \frac{1}{3}(\tilde{\theta}_1 + \tilde{\theta}_2 + \tilde{\theta}_3)$ and $\theta_i' = \tilde{\theta}_i - \bar{\theta}$. Consequently $\theta_1' + \theta_2' + \theta_3' = 0$. The deviatoric corner rotations define the linear deviatoric-rotation field:

$$\theta' = \theta_1'\zeta_1 + \theta_2'\zeta_2 + \theta_3'\zeta_3, \tag{3.18}$$

which integrates to zero over the element. The splitting of hierarchical rotations translates to a similar decomposition of the higher order strains: $\mathbf{e}_d = \mathbf{e}_b + \mathbf{e}_t$, where subscript 'b' and 't' identify "pure bending" and "torsional" strain fields, respectively. These are generated by the deviatoric rotations θ' and the mean hierarchical rotation $\bar{\theta}$, respectively.

3.4 The Stiffness Template

An acceptable template fulfills the following conditions:

(C) Consistency: the Individual Element Test (IET) form of the patch test, introduced by Bergan and Hanssen [42, 43], is passed for any element geometry. The IET is a strong form of the patch test that demands pairwise cancellation of tractions between adjacent elements in constant stress states.

(S) Stability: the stiffness matrix satisfies correct rank and nonnegativity conditions.

(P) Parametrization: the element stiffness equations contain free parameters.

(I) Invariance: the element equations are observer invariant. In particular, they are independent of node numbering and choice of reference systems.

The first two conditions: (C) and (S), are imposed to ensure convergence as the mesh size is reduced by enforcing *a priori* satisfaction of the IET. Property (P)

permits performance optimization as well as tuning elements to custom needs. Property (I) helps predictability and benchmark testing.

The fundamental element stiffness decomposition of the two-stage direct fabrication method of HP elements is

$$\mathbf{K} = \mathbf{K}_b + \mathbf{K}_h. \tag{3.19}$$

Here $\mathbf{K}_\mathrm{b}$ is the basic stiffness, which takes care of consistency, and $\mathbf{K}_\mathrm{h}$ is the higher order stiffness, which takes care of stability (rank sufficiency) and accuracy. This decomposition was found by Bergan and Nygard [10] as part of the Free Formulation (FF), but actually holds for any element that passes the individual element test (IET) of Bergan and Hanssen [42, 43]. In addition $\mathbf{K}_\mathrm{h}$ need to satisfy certain orthogonality conditions.

The ANDES triangles derived in [17] initially carry along a set of free numerical parameters, most of which affect the higher order stiffness:

$$\mathbf{K}^{ANDES}(\alpha_b, \beta, \rho_1, ..., \rho_5) = \mathbf{K}_b(\alpha_b) + \beta \mathbf{K}_h^u(\rho_1, ..., \rho_5), \tag{3.20}$$

where $\mathbf{K}_h^u$ is the unscaled higher order stiffness. Both $\mathbf{K}_\mathrm{b}$ and $\mathbf{K}_\mathrm{h}$ must have rank 3. Parameters β and ρ_i are renamed in the development of a more general template in Section 3.4.2. Algebraic forms such as Eq. (3.20) possessing free parameters are called *element stiffness templates*.

3.4.1 The Basic Stiffness

An explicit form of the basic stiffness for the LST-3/9R configuration was obtained in 1984 and published the following year [5]. It can be expressed as

$$\mathbf{K}_b = V^{-1}\mathbf{L}\mathbf{E}\mathbf{L}^T, \tag{3.21}$$

Where $V = Ah$ is the element volume, and $\mathbf{L}$ is a 9×3 matrix that contains a free parameter α_b :

$$\mathbf{L} = \frac{1}{2}h\begin{bmatrix} y_{23} & 0 & x_{32} \\ 0 & x_{32} & y_{23} \\ \frac{1}{6}\alpha_b y_{23}(y_{13}-y_{21}) & \frac{1}{6}\alpha_b x_{32}(x_{31}-x_{12}) & \frac{1}{3}\alpha_b(x_{31}y_{13}-x_{12}y_{21}) \\ y_{31} & 0 & x_{13} \\ 0 & x_{13} & y_{31} \\ \frac{1}{6}\alpha_b y_{31}(y_{21}-y_{32}) & \frac{1}{6}\alpha_b x_{13}(x_{12}-x_{23}) & \frac{1}{3}\alpha_b(x_{12}y_{21}-x_{23}y_{32}) \\ y_{12} & 0 & x_{21} \\ 0 & x_{21} & y_{12} \\ \frac{1}{6}\alpha_b y_{12}(y_{32}-y_{13}) & \frac{1}{6}\alpha_b x_{21}(x_{23}-x_{31}) & \frac{1}{3}\alpha_b(x_{23}y_{32}-x_{31}y_{13}) \end{bmatrix}. \tag{3.22}$$

The basic stiffness $\mathbf{K}_{\mathrm{b}}(\alpha_b)$ is identical for both EFF and ANDES formulations. In fact, patch test and template theory says that $\mathbf{K}_{\mathrm{b}}(\alpha_b)$ must be shared by all elements with this node-freedom configuration that pass the IET although α_b may vary for different models. However α_b must be the same for all LST-3/9R elements connected in an assembly, for otherwise the IET would be violated. Parameters other than α_b, such as β and ρ_i in Eq. (3.20), may, in principle, vary from element to element without affecting convergence.

3.4.2 The Higher Order Stiffness

We describe here essentially the ANDES form of $\mathbf{K}_{\mathrm{h}}$ developed in [17], with some generalizations in the set of free parameters discussed at the end of this subsection. The higher order stiffness matrix is

$$\mathbf{K}_h = c_{fac}\,\widetilde{\mathbf{T}}_{\theta u}^T \mathbf{K}_\theta \widetilde{\mathbf{T}}_{\theta u}, \tag{3.23}$$

Where $\mathbf{K}_\theta$ is the 3×3 higher order stiffness in terms of the hierarchical rotations $\tilde{\theta}$ of (3.13), $\widetilde{\boldsymbol{T}}_{\theta u}$ is the matrix in Eq. (3.15), and c_{fac} is a scaling factor to be determined later. To construct $\mathbf{K}_\theta$ by ANDES we picks deviatoric natural strain patterns, in which "deviatoric" means change from the constant strain states.

To express $\mathbf{K}_\theta$ compactly, introduce the following matrices, which depend on nine free dimensionless parameters, β_1 through β_9:

$$\mathbf{Q}_1 = \frac{2A}{3}\begin{bmatrix} \frac{\beta_1}{\ell_{21}^2} & \frac{\beta_2}{\ell_{21}^2} & \frac{\beta_3}{\ell_{21}^2} \\ \frac{\beta_4}{\ell_{32}^2} & \frac{\beta_5}{\ell_{32}^2} & \frac{\beta_6}{\ell_{32}^2} \\ \frac{\beta_7}{\ell_{13}^2} & \frac{\beta_8}{\ell_{13}^2} & \frac{\beta_9}{\ell_{13}^2} \end{bmatrix}, \quad \mathbf{Q}_2 = \frac{2A}{3}\begin{bmatrix} \frac{\beta_9}{\ell_{21}^2} & \frac{\beta_7}{\ell_{21}^2} & \frac{\beta_8}{\ell_{21}^2} \\ \frac{\beta_3}{\ell_{32}^2} & \frac{\beta_1}{\ell_{32}^2} & \frac{\beta_2}{\ell_{32}^2} \\ \frac{\beta_6}{\ell_{13}^2} & \frac{\beta_4}{\ell_{13}^2} & \frac{\beta_5}{\ell_{13}^2} \end{bmatrix}, \quad \mathbf{Q}_3 = \frac{2A}{3}\begin{bmatrix} \frac{\beta_5}{\ell_{21}^2} & \frac{\beta_6}{\ell_{21}^2} & \frac{\beta_4}{\ell_{21}^2} \\ \frac{\beta_8}{\ell_{32}^2} & \frac{\beta_9}{\ell_{32}^2} & \frac{\beta_7}{\ell_{32}^2} \\ \frac{\beta_3}{\ell_{13}^2} & \frac{\beta_1}{\ell_{13}^2} & \frac{\beta_2}{\ell_{13}^2} \end{bmatrix}. \quad (3.24)$$

Matrix $\mathbf{Q}_i$ relates the natural strains $\boldsymbol{\epsilon}_i$ at corner i to the deviatoric corner curvatures $\widetilde{\boldsymbol{\theta}}$. At a point of triangular coordinates $\{\zeta_1, \zeta_2, \zeta_3\}$, $\boldsymbol{\epsilon} = \mathbf{Q}\widetilde{\boldsymbol{\theta}}$, where $\mathbf{Q} = \mathbf{Q_1}\zeta_1 + \mathbf{Q_2}\zeta_2 + \mathbf{Q_3}\zeta_3$. Evaluate this at the midpoints:

$$\mathbf{Q}_4 = \frac{1}{2}(\mathbf{Q}_1 + \mathbf{Q}_2), \quad \mathbf{Q}_5 = \frac{1}{2}(\mathbf{Q}_2 + \mathbf{Q}_3), \quad \mathbf{Q}_6 = \frac{1}{2}(\mathbf{Q}_3 + \mathbf{Q}_1). \quad (3.25)$$

Then

$$\mathbf{K}_\theta = h(\mathbf{Q}_4^T\mathbf{E}_{nat}\mathbf{Q}_4 + \mathbf{Q}_5^T\mathbf{E}_{nat}\mathbf{Q}_5 + \mathbf{Q}_6^T\mathbf{E}_{nat}\mathbf{Q}_6), \quad (3.26)$$

and $\mathbf{K}_h = \frac{3}{4}\beta_0\mathbf{T}_{\theta u}^T\mathbf{K}_\theta\mathbf{T}_{\theta u}$, where β_0 is an overall scaling coefficient. So finally $\mathbf{K_R}$ assumes a template form with 11 free parameters $\alpha_b, \beta_0, \beta_1, \ldots, \beta_9$:

$$\mathbf{K}_R(\alpha_b, \beta_0, \beta_1, \ldots, \beta_9) = V^{-1}\mathbf{L}\mathbf{E}\mathbf{L}\mathbf{L}^T + \frac{3}{4}\beta\widetilde{\mathbf{T}}_{\theta u}^T\mathbf{K}_\theta\widetilde{\mathbf{T}}_{\theta u}. \quad (3.27)$$

The template (3.27) is the "LST-3/9R ANDES stiffness template". Note the parameter set used in (3.27) is more general than that used in [17]. That template carried only five free parameters in the matrices: ρ_1 through ρ_5, which automatically enforced the triangular symmetry conditions

$$\beta_7 = -\beta_1, \quad \beta_8 = -\beta_3, \quad \beta_9 = -\beta_2. \tag{3.28}$$

By solving a set of polynomial equations for template optimality, the parameter set is given as:

$$\alpha_b = \tfrac{3}{2}, \quad \beta_0 = \tfrac{1}{2}, \quad \beta_1 = \beta_3 = \beta_5 = 1, \quad \beta_2 = 2, \quad \beta_4 = 0, \quad \beta_6 = \beta_7 = \beta_8 = -1, \quad \beta_9 = -2. \tag{3.29}$$

This solution is worked out in Appendix B. of [3]. Replacing these values in (3.27) we obtain a stiffness matrix instance of LST-3/9R labeled as OPT (for optimum) in [3]. Table 2 from [3] defines the signatures of listed triangular element if they happen to be instances of the ANDES template (3.27). The signatures of CST and OPT element will be used towards the results in Chapter 4.

Table 2 [3]. Signatures of some LST-3/9R instances befitting the ANDES template

Name	α_b	β_0	β_1	β_2	β_3	β_4	β_5	β_6	β_7	β_8	β_9
ALL-3I	1	4/9	1/12	5/12	1/2	0	1/3	−1/3	−1/12	−1/2	−5/12
ALL-3M	1	4/9	1/4	5/4	3/2	0	1	−1	−1/4	−3/2	−5/4
ALL-EX	not an instance of ANDES template										
ALL-LS	1	4/9	3/20	3/4	9/10	0	3/5	−3/5	−3/20	−9/10	−3/4
CST	0	any	0	0	0	0	0	0	0	0	0
FF84	not an instance of ANDES template										
LST-Ret	4/3	1/2	2/3	−2/3	0	0	−4/3	4/3	−2/3	0	2/3
OPT	3/2	see §5.2	1	2	1	0	1	−1	−1	−1	−2

3.5 The Mass Template

As mentioned in the mass construction method section, the matrix-weighted parametrization technique is used in the thesis for construction of mass template. The simplest template has the form of Eq. (2.6), which contain just one free combination parameter μ.

3.5.1 Lumped Mass Matrices for CST and LST-3/9R

For CST membrane element, also known as the plane stress linear triangle, a diagonally lumped mass matrix (DLMM) is readily obtained as follows. Assume constant mass density ρ, area A, uniform thickness h, and that the motion is restricted to the $\{x, y\}$ plane. The six DOFs are arranged as $\mathbf{u}^e = \left[u_{x1}\ u_{y1}\ u_{x2}\ u_{y2}\ u_{x3}\ u_{y3}\right]^T$. The DLMM is constructed by taking the total mass of the element, which is ρAh, deviding it by 3 and assigning those to the corner nodes. See Figure 6. This process produces a diagonal matrix:

$$\mathbf{M}_L^e = \frac{\rho Ah}{3}\text{diag}\left[1 \quad 1 \quad 1 \quad 1 \quad 1 \quad 1\right] = \frac{\rho Ah}{3}\mathbf{I}_6, \tag{3.30}$$

in which $\mathbf{I}_6$ denotes the identity matrix of order 6. The same matrix is obtained by any other diagonalization method, for example the HRZ scheme described in Section 1.1.3.

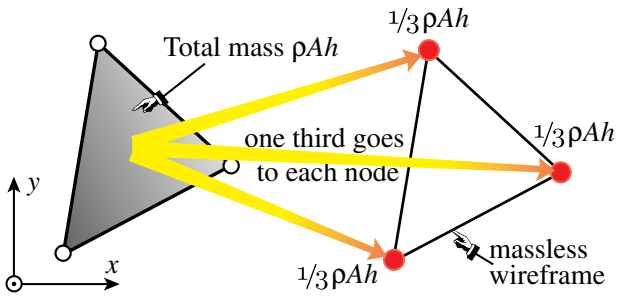

Figure 6. DLMM for 3-node triangular element.

For the plane stress linear triangle with rotational DOF at each corner, the same procedure can be used to obtain the DLMM. The translational nodal masses must be the same as that of previous triangle: $\rho Ah/3$. But the rotational masses are set to zero. Therefore,

$$\mathbf{M}_L^e = \frac{\rho Ah}{3}\,\mathrm{diag}\begin{bmatrix}1 & 1 & 0 & 1 & 1 & 0 & 1 & 1 & 0\end{bmatrix}. \tag{3.31}$$

3.5.2 Quasi-Consistent Mass for LST-3/9R

As noted in Chapter 2, the consistent mass matrix (CMM) of a displacement-assumed finite element is conventionally obtained by injecting the element shape function used for the stiffness matrix into the kinetic energy functional and taking the Hessian with respect to its DOF. This straight forward process is difficult to follow for the LST-3/9R element because of two attendant complications:

(I) The element stiffness is developed using assumed natural strains rather than displacements.

(II) Although the assumed strains can be analytically integrated upon transforming to Cartesian components, the resulting displacement functions are

complicated and carry several free parameters. It was felt that a thorough analysis would take excessive time for a report to be prepared.

Overcoming these difficulties may have taken a significant amount of time, even with computer algebra help. To expedite the derivation, a simplified "divide and conquer" was taken. A decomposition similar to that used to derive the stiffness template was used to build a "quasi-consistent" mass matrix, or QCMM. The QCMM is obtained as the sum of the CMM of the CST element and higher order consistent mass M_θ relating hierarchical rotations. This is expressed as:

$$\mathbf{M}_{QC} = \mathbf{M}_{CST} + (\widetilde{\mathbf{T}}_{\theta u})^T \mathbf{M}_\theta \widetilde{\mathbf{T}}_{\theta u}, \tag{3.32}$$

in which $\mathbf{M}_{CST}$ is the well-known 6×6 CMM for the CST in [44]. By adding extra zero rows and columns we expand it to a 9×9 matrix, assuming zero masses related with rotational DOFs, which yields

$$M_{CST} = \frac{\rho A h}{12} \begin{bmatrix} 2 & 0 & 0 & 1 & 0 & 0 & 1 & 0 & 0 \\ 0 & 2 & 0 & 0 & 1 & 0 & 0 & 1 & 0 \\ 0 & 0 & 0 & 0 & 0 & 0 & 0 & 0 & 0 \\ 1 & 0 & 0 & 2 & 0 & 0 & 1 & 0 & 0 \\ 0 & 1 & 0 & 0 & 2 & 0 & 0 & 1 & 0 \\ 0 & 0 & 0 & 0 & 0 & 0 & 0 & 0 & 0 \\ 1 & 0 & 0 & 1 & 0 & 0 & 2 & 0 & 0 \\ 0 & 1 & 0 & 0 & 1 & 0 & 0 & 2 & 0 \\ 0 & 0 & 0 & 0 & 0 & 0 & 0 & 0 & 0 \end{bmatrix}. \tag{3.33}$$

$\mathbf{M}_\theta$ is the 9×9 higher order consistent mass in terms of the hierarchical rotations $\tilde{\theta}$ of (3.13), $\widetilde{\boldsymbol{T}}_{\theta u}$ is the matrix in Eq. (3.15). $\mathbf{M}_\theta$ can be calculated using Eq. (2.4):

$$\mathbf{M}_\theta = \int_{\Omega^e} \rho (\mathbf{N}^e_{\theta z})^T \mathbf{N}^e_{\theta z} d\Omega, \tag{3.34}$$

where $\boldsymbol{N}_{\theta z}$ is the shape function matrix of hierarchical rotations.

$$N_{\theta z}^{T}=\begin{bmatrix} -\zeta_1^2(y_{21}\zeta_2-y_{13}\zeta_3)+(y_{13}-y_{21})\zeta_1\zeta_2\zeta_3/2 & -\zeta_1^2(x_{21}\zeta_2-x_{13}\zeta_3)+(x_{13}-x_{21})\zeta_1\zeta_2\zeta_3/2 \\ -\zeta_2^2(y_{32}\zeta_3-y_{21}\zeta_1)+(y_{21}-y_{32})\zeta_1\zeta_2\zeta_3/2 & -\zeta_2^2(x_{32}\zeta_3-x_{21}\zeta_1)+(x_{21}-x_{32})\zeta_1\zeta_2\zeta_3/2 \\ -\zeta_3^2(y_{13}\zeta_1-y_{32}\zeta_2)+(y_{32}-y_{13})\zeta_1\zeta_2\zeta_3/2 & -\zeta_3^2(x_{13}\zeta_1-x_{32}\zeta_2)+(x_{32}-x_{13})\zeta_1\zeta_2\zeta_3/2 \end{bmatrix}.$$

(3.35)

Plots of shape functions for rotational DOF of each corner are shown in Figure 7. Also the bending mode (a) and torsion mode (b) are shown in Figure 8. They give us a better and direct understanding of the role of these shape function in capturing higher order hierarchical motions.

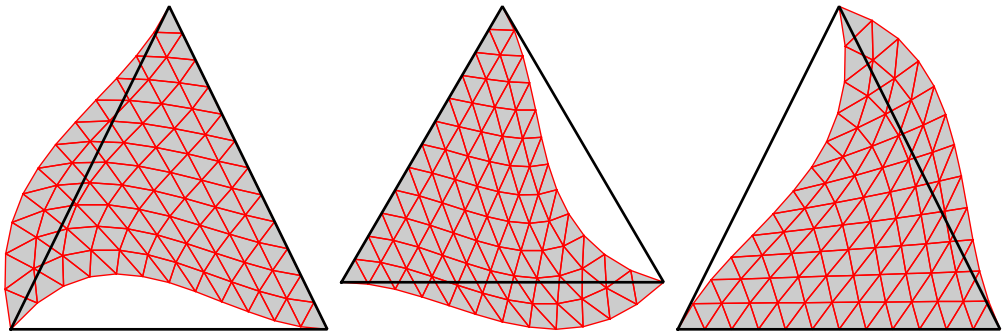

Figure 7. Shape funtions for rotational DOF of each corner

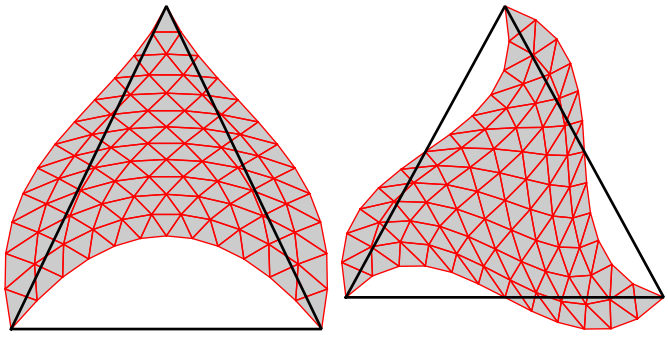

(a) (b)

Figure 8. The bending mode and the torsion mode

CHAPTER 4

NUMERICAL RESULTS AND DISCUSSION

This Chapter presents and discusses numerical results for the dispersion analysis of two specific membrane (plane stress) elements.

1. CST-3/6C. The conventional constant strain triangle or CST, also called the linear-displacement triangle and Turner triangle in the FEM literature. It has 3 corner nodes and 6 DOF.

2. LST-3/9R. The linear strain element with drilling freedoms, described in the previous Chapter. This element is used as membrane component of a shell triangular element used in several FEM programs around the world, notably the SALINAS code of Sandia.

These two elements are depicted in Figure 9. They will be often referred as CST and LST, respectively, for brevity.

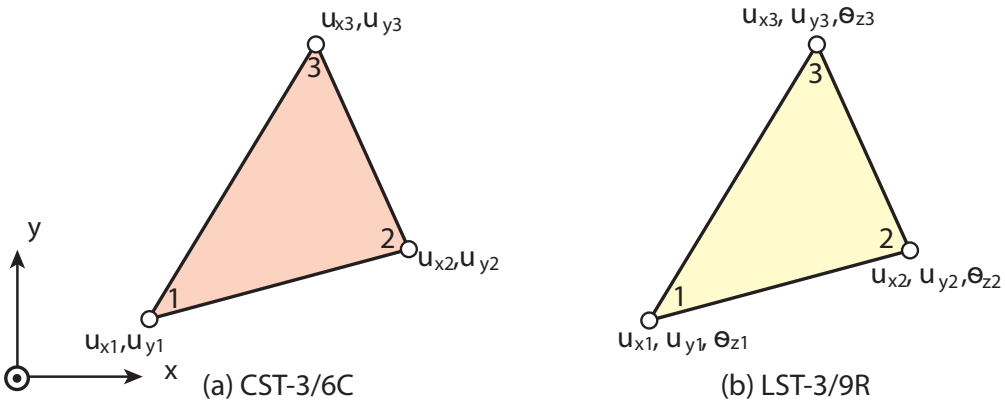

Figure 9. Configuration of the membrane triangle (a) CST-3/6C and (b) LST-3/9R.

4.1 Wave Propagation Over Lattices

The dispersion analysis is carried out over regular infinite lattices formed by the two elements described above. For expediency, this work considered only square-cell lattices and an isotropic material.

To study the effect of wave directionality, the direction of propagation of the P-wave and S-wave was allowed to form an angle ϕ with the lattice principal direction. This was implemented as shown in Figure 10: While the wave direction is always x, the lattice was rotated by an angle ϕ with respect to that axis.

The dispersion analysis method described in Chapter 2 was used. Best parameters of mass matrices were obtained for different Poisson's ratio ν and different rotational angles ϕ. Dispersion curves obtained with specific mass matrices for P-wave and S-wave are shown separately in the results reported in subsequent sections. Comparisons between discrete and continuum plate in the low frequency range are also included.

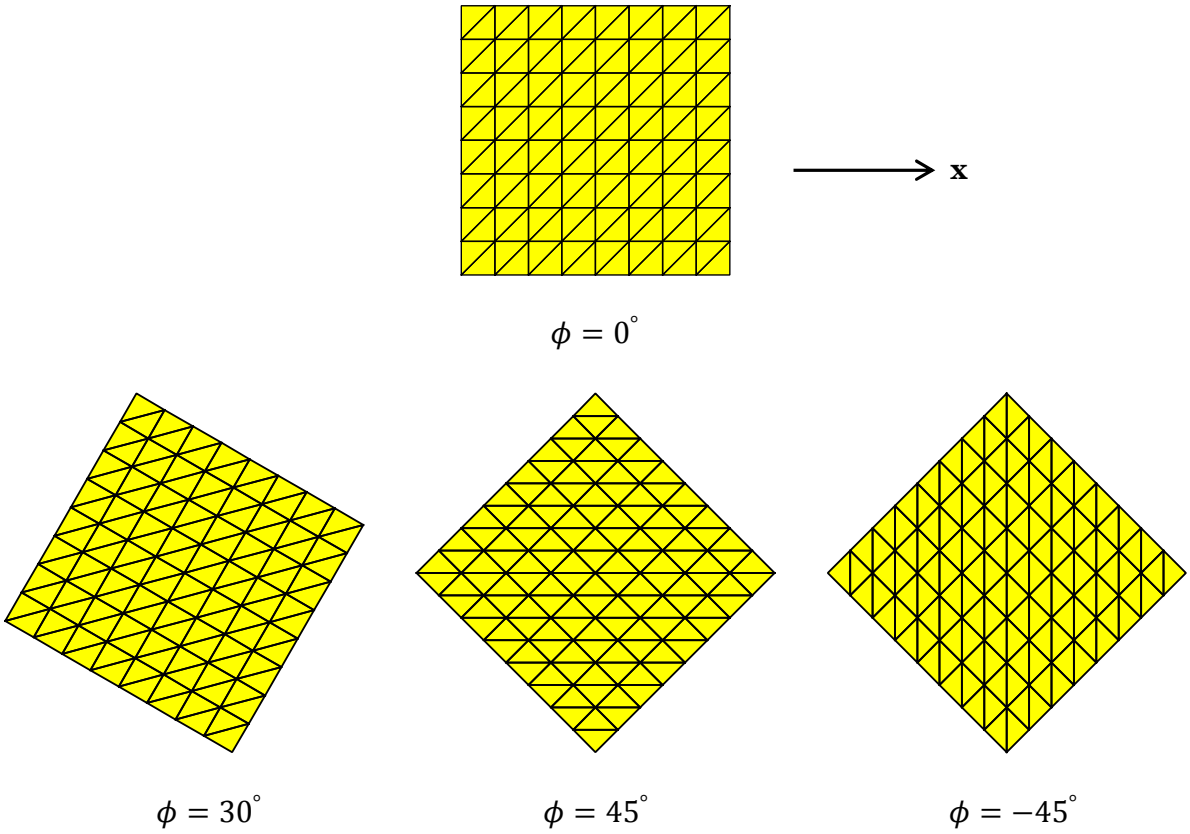

Figure 10. Finite element mesh plots of infinite plate with respect to different rotational angles. Wave direction is always along the x axis.

4.2 Constant Strain Triangle Element

This section presents results obtained for the CST element.

4.2.1 Best μ by Taylor Expansion

As described in Chapter 2, plane wave residuals over a finite element patch of CST elements are obtained from the matrix-vector product

$$\{r_x, r_y, r_\theta\}^T = (\mathbf{K}_p - \omega^2 \mathbf{M}_p)\mathbf{u}_p \tag{4.1}$$

For the P-wave, $B_y = 0, u_y = 0$, and by requiring $r_x = 0$ we solve for $\omega_p^2(k)$. For the S-wave, $B_x = 0, u_x = 0$, and by requiring $r_y = 0$ we solve for $\omega_s^2(k)$. They are the dispersion relations. These are then Taylor expanded in powers of k about $k = 0$,

including terms up to k^4. These frequencies are in the long wavelength limit. Since the Taylor expansion expression for ω_s^2 is complicated, we take the P-wave here as an example to show the complete process. For the CST element lattice,

$$\omega_p^2 = \frac{E_m k^2}{\rho - \nu^2 \rho} + \frac{a^2 E_m k^4 (-34 + 64\mu + 6\nu + (2 - 6\nu)\cos(4\phi) + (-23 + 32\mu + 9\nu)\sin(2\phi) - (3 + 3\nu)\sin(6\phi))}{384(-1 + \nu^2)\rho}. \tag{4.2}$$

The general dispersion expression for a regular FEM lattice is

$$\omega_{FEM}^2 = c_0^2 k^2 + Dk^4 + O(k^6), \tag{4.3}$$

in which $c_0^2 = E_m/\rho(1 - \nu^2)$ for the P-wave, $c_0^2 = E_m/2\rho(1 + \nu)$ for the S-wave.

For a continuum isotropic media, the group velocity is $c_0 = \omega/k$, or $\omega^2 = c_0^2 k^2$. Eq. (4.3) indicates that as k->0 the FEM dispersion expression approaches the continuum one with second-order relative error $Dk^2/{c_0}^2$.

The FEM-over-continuum frequency ratio truncated to 2 terms is

$$\omega_{rat}^2 = \frac{\omega_{FEM}^2}{\omega_{con}^2} = 1 + \frac{D}{c_0^2} k^2. \tag{4.4}$$

The relative frequency error is

$$\omega_{err}^2 = (\omega_{rat}^2 - 1)/k^2 = D/c_0^2, \tag{4.5}$$

in which the coefficient D is a function of the propagation angle ϕ, Poisson's ratio ν and mass combination coefficient μ.

It is of interest to find a value of μ, called μ_{opt}, that minimizes $|D|$ in some sense. The mass matrix obtained with that particular value is called a best low-frequency mass matrix (BLFMM). For the P-wave of CST element, Eq. (4.5) becomes

$$\omega_{err}^2 = \frac{a^2}{384}(34 - 64\mu - 6\nu + (6\nu - 2)\cos(4\phi) + (23 - 32\mu - 9\nu)\sin(2\phi) + 3(1+\nu)\sin(6\phi)). \quad (4.6)$$

Setting $\omega_{err}^2 = 0$, or equivalently $D = 0$, we obtain a relation $\mu_{opt} = \mu_{opt}(\nu, \phi)$, whence the value of μ_{opt} depends on ν and ϕ. By averaging ϕ over the range [-π/2, π/2], and ν over the range [0,1/2], we obtain the μ_{opt} for CST element for P-wave propagation plotted in Figure 11. We can directly read from the figure, that when $\phi = 0$, $\mu = 1/2$, which is independent of ν; when $\phi = \pi/4$, $\mu = \frac{1}{12}(7 - 3\nu)$.

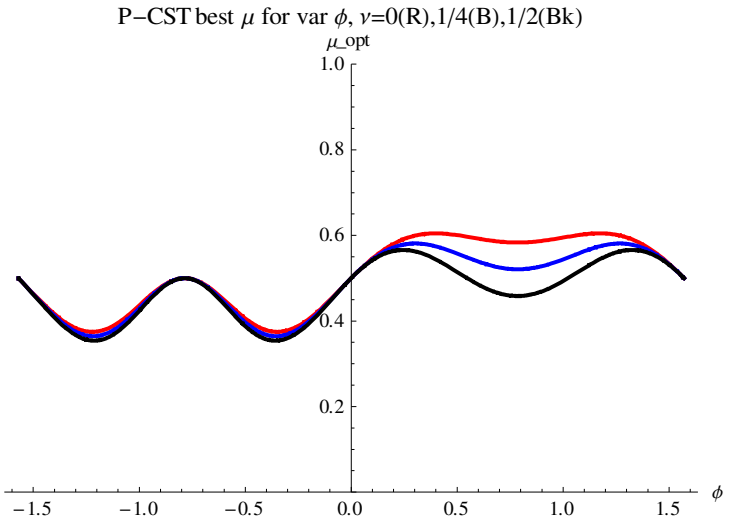

Figure 11. Best u for the P-wave, CST element over $\phi \in [-\pi/2, \pi/2]$ for Poisson's ratios ν=0(R), 0.25(B), 0.5(Bk)

We can obtain the μ_{opt} of the CST element for S-wave propagation by the same procedure. The result is shown in Figure 12.

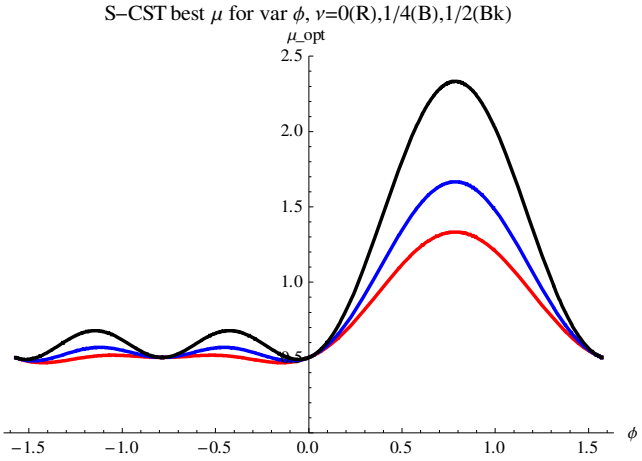

Figure 12. Best u for the S-wave, CST element over $\phi \in [-\pi/2, \pi/2]$ for Poisson's ratios ν=0(R), 0.25(B), 0.5(Bk)

Since the angle ϕ is not often known in advance, it is convenient to get an average value of μ_{opt} for different Poisson's ratios. For that we integrate μ_{opt} over $\phi \in [-\pi/2, \pi/2]$, and divide by π, we obtain

$$\mu_{opt}^{avg}(\nu) = \frac{1}{48}(-45 + 40\sqrt{3} - 45\nu + 24\sqrt{3}\nu) \text{ for P-wave, } \frac{45 - 16\sqrt{3} + 45\nu - 32\sqrt{3}\nu}{24 - 24\nu} \text{ for S-wave.}$$

(4.7)

This is plotted for different Poisson's ratios $\nu \in [0,1/2]$, in Figure 13. It can be observed that the dependence of this ϕ-averaged μ_{opt} on ν is mild. The average μ_{opt} for the P-wave is around 0.5, whereas for the S-wave it is around 0.75~0.8. Insert μ_{opt} into Eq. (2.6) we obtain the BLFMM for a general wave propagation problem.

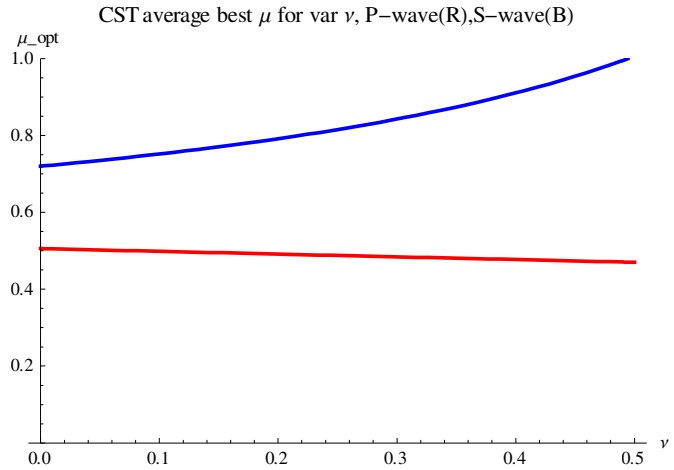

Figure 13. CST average best μ for $\nu \in [0,1/2]$, P-wave(R), S-wave(B)

4.2.2 The P-wave for CST

As for P-wave, $r_x = 0$. The plot of r_y with respect to various ϕ is shown in Figure 14. Here r_y is independent of μ and ω. When $\phi = 0^\circ$ and $\phi = 45^\circ, r_y = 0$. This means these cases corresponds to the exact plane wave propagation. Other cases where $r_y \neq 0$, means that the plane wave propagation is distorted by the FEM discretization, even for a regular lattice.

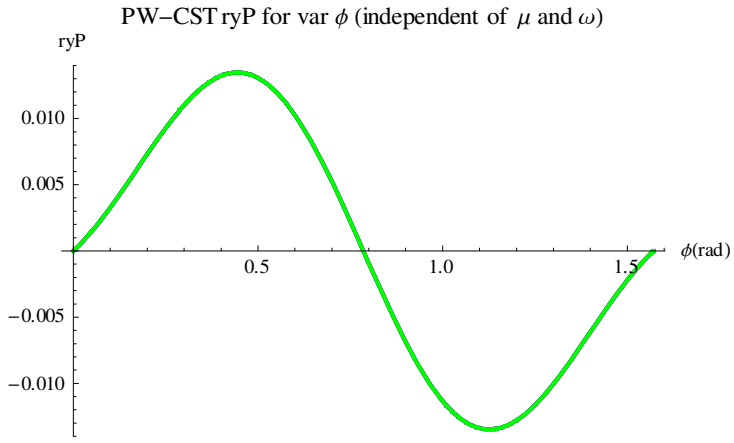

Figure 14. Residual in y axis with various ϕ for P-wave in CST element.

From Figure 11 we can get the best μ for various rotational angles and Poison ratios. For the representative angles ($\phi = 0^{\circ}, 45^{\circ}, 45^{\circ}, 30^{\circ}$) and Poison ratios ($\nu = 0, 0.5$) that we are interested in, the value of best μ is shown in Table 3.

Table 3. Best μ for P-wave in CST for various ϕ and ν

μ_{opt} / ϕ / υ	0°	45°	-45°	30°
0	0.5	0.6	0.5	0.6
0.5	0.5	0.45	0.5	0.5

Inserting these μ_{opt} into the mass template, plus the well-known stiffness matrix, we got the dispersion curves for CMM, DLMM and BLFMM respectively, for different poison ratio ($\nu = 0, \nu = 0.5$) and different mesh orientations ($\phi = 0^{\circ}, 45^{\circ}, -45^{\circ}, 30^{\circ}$) as shown in Figure 15-18. The dispersion relation of the continuum $\omega_{con}(k)$ is also shown for matching with finite element results in the low frequency range. We can observe that the dispersion curves using BLFMM match the continuum better than those for DLMM and CMM in all cases, for the long wavelength limit.

To show the exact error, we plot the error in low frequency range $k \in [0, \pi/3]$ between the continuum and each discrete case, that is $\omega_p - \omega_{con}$. They are shown on the right hand of each dispersion curves. It is obvious the error for the BLFMM is almost zero everywhere. The CMM and DLMM show larger errors in different directions.

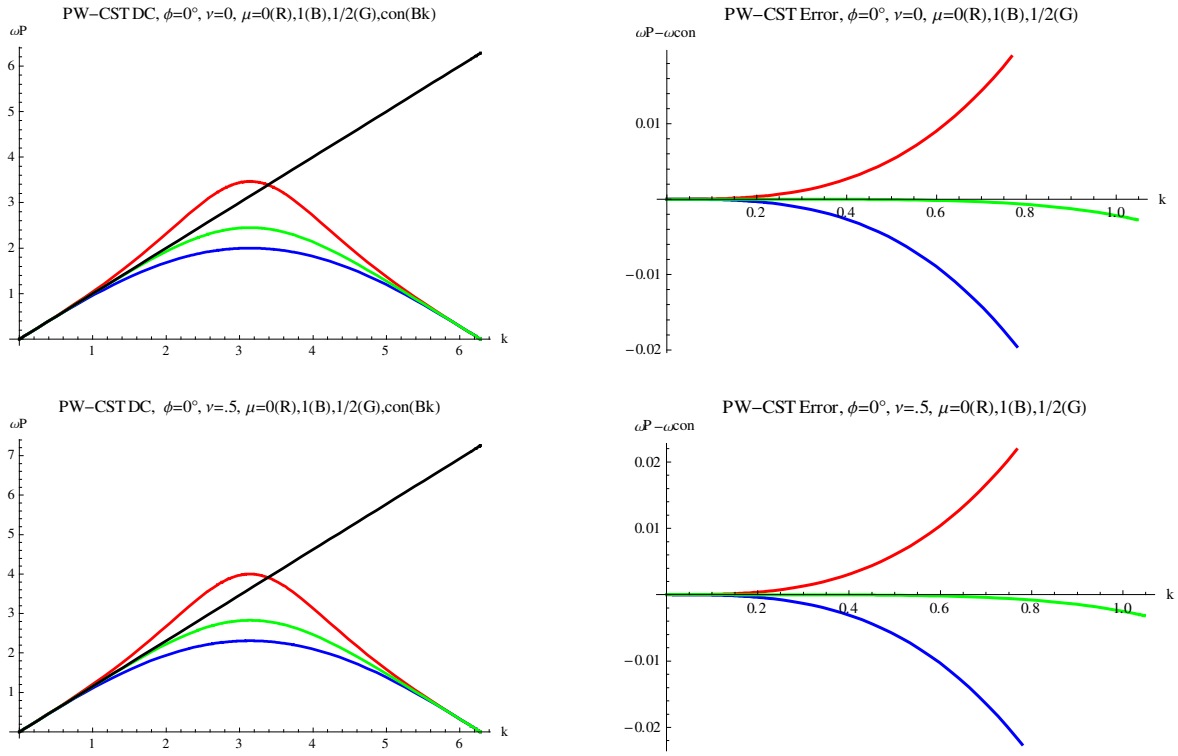

Figure 15. Dispersion curves for P-wave in CST element ($\phi = 0^{\circ}$), CMM (R), DLMM(B), BLFMM(G), continuum (Bk)

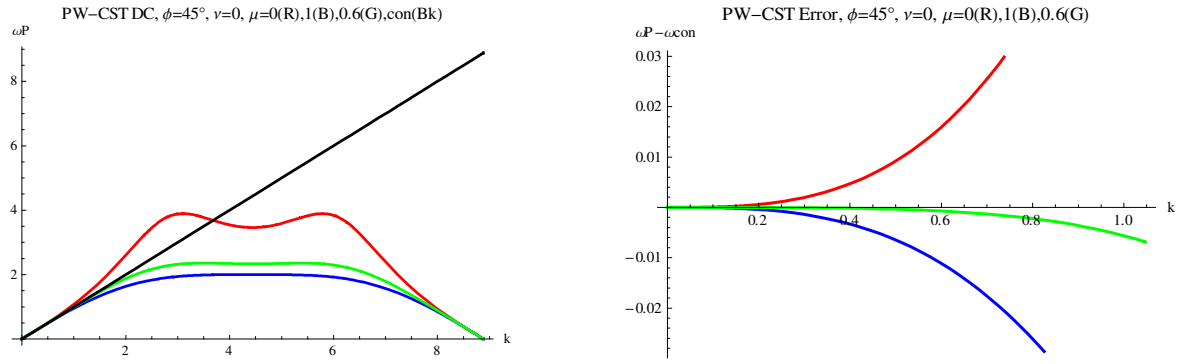

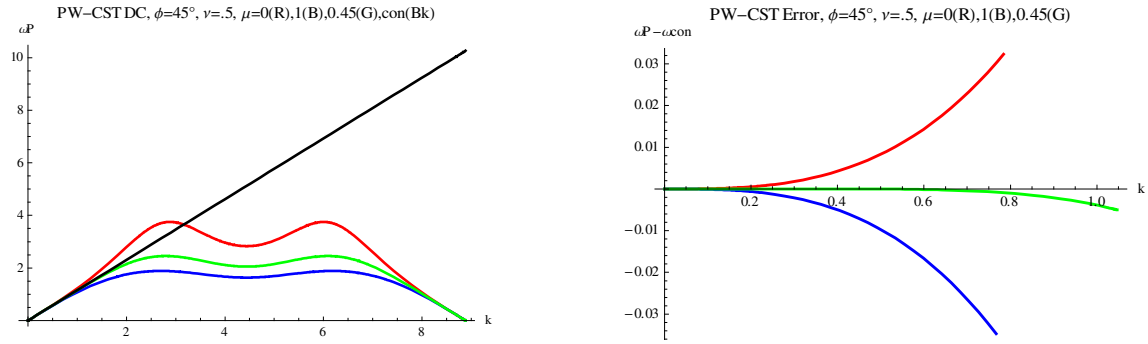

Figure 16. Dispersion curves for P-wave in CST element ($\phi = 45^{\circ}$),CMM (R), DLMM(B), BLFMM(G), continuum (Bk)

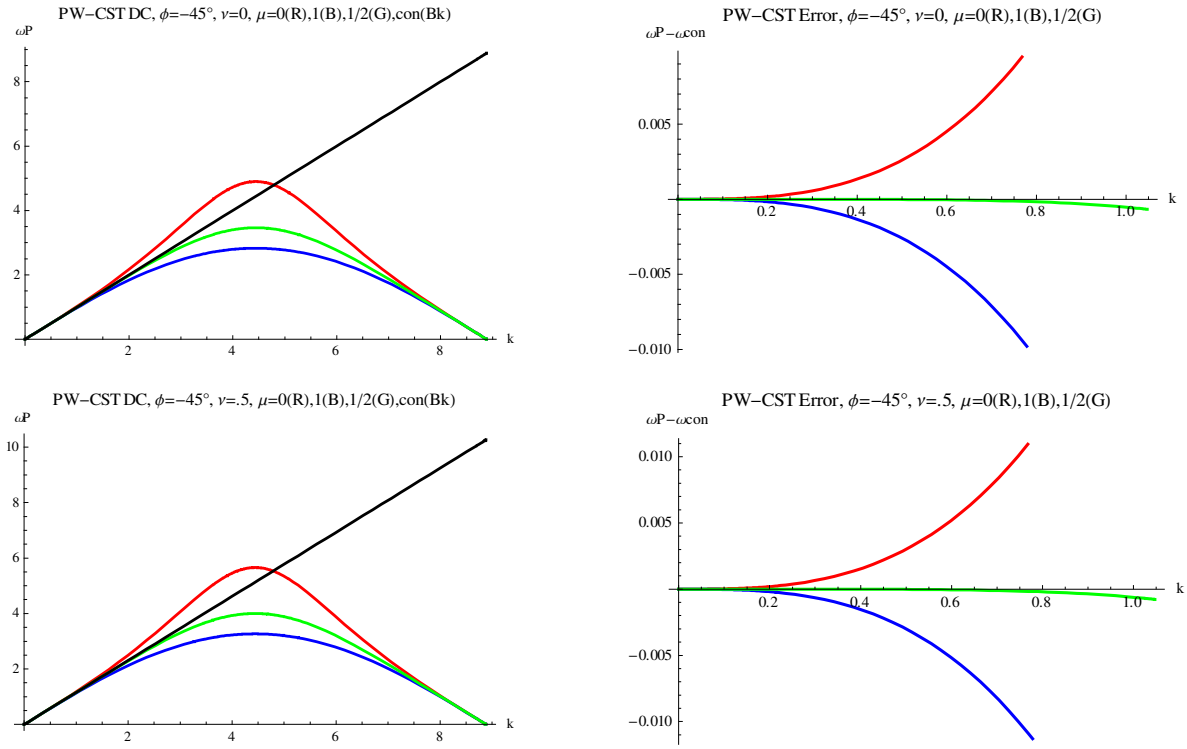

Figure 17. Dispersion curves for P-wave in CST element ($\phi = -45^{\circ}$),CMM (R), DLMM(B), BLFMM(G), continuum (Bk)

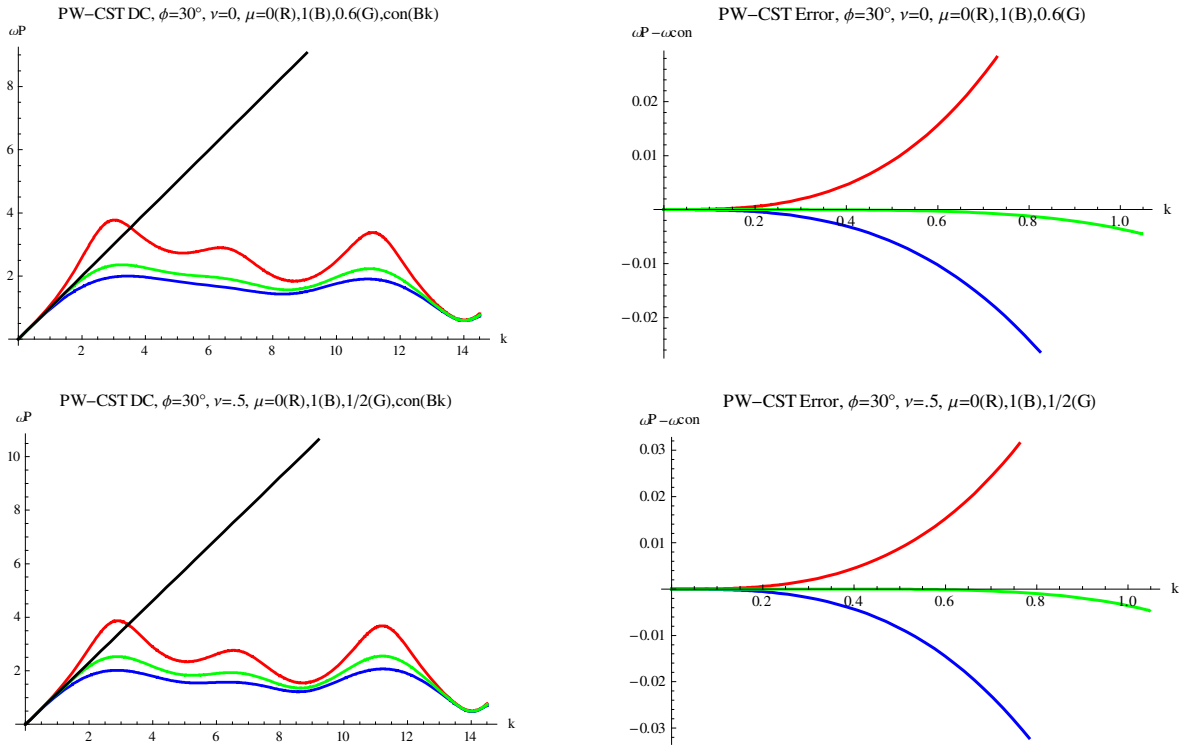

Figure 18. Dispersion curves for P-wave in CST element ($\phi = 30^{\circ}$),CMM (R), DLMM(B), BLFMM(G), continuum (Bk)

4.2.3 The S-wave for CST

Similarly, for the S-wave we enforce $r_y = 0$. The plot of the risidual r_x for variable ϕ in range [0, 90°] is shown in Figure 19. Here r_x is independent of μ and ω. When $\phi = 0^{\circ}$ and $\phi = 45^{\circ}, r_y = 0$. This means that in those cases the plane wave is not distorted by the FEM discretization.

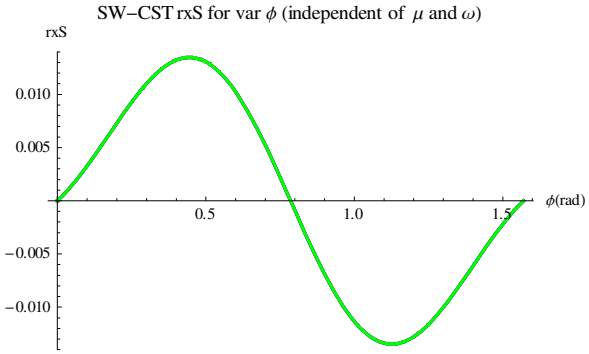

Figure 19. Residual in x axis with various ϕ for S-wave in CST element.

From Figure 12 we can get the best μ for various rotational angles and Poisson's ratios. We are interested in $\phi = 0^{\circ}, 45^{\circ}, -45^{\circ}$ and $\nu = 0,\ 0.5$. The value of best μ is shown in Table 4. Note when $\phi = 45^{\circ}$, $\mu_{opt} > 1$, which is different from that of other angles.

Table 4. Best μ for S-wave in CST for various ϕ and ν

μ_{opt} ϕ / υ	0°	45°	-45°
0	0.5	1.3	0.5
0.5	0.5	2.5	0.5

The same dispersion curves comparison as P-wave are shown in Figure 20-22. The same conclusion can be made that the error for the BLFMM is almost zero everywhere. The CMM and DLMM show larger errors in different directions.

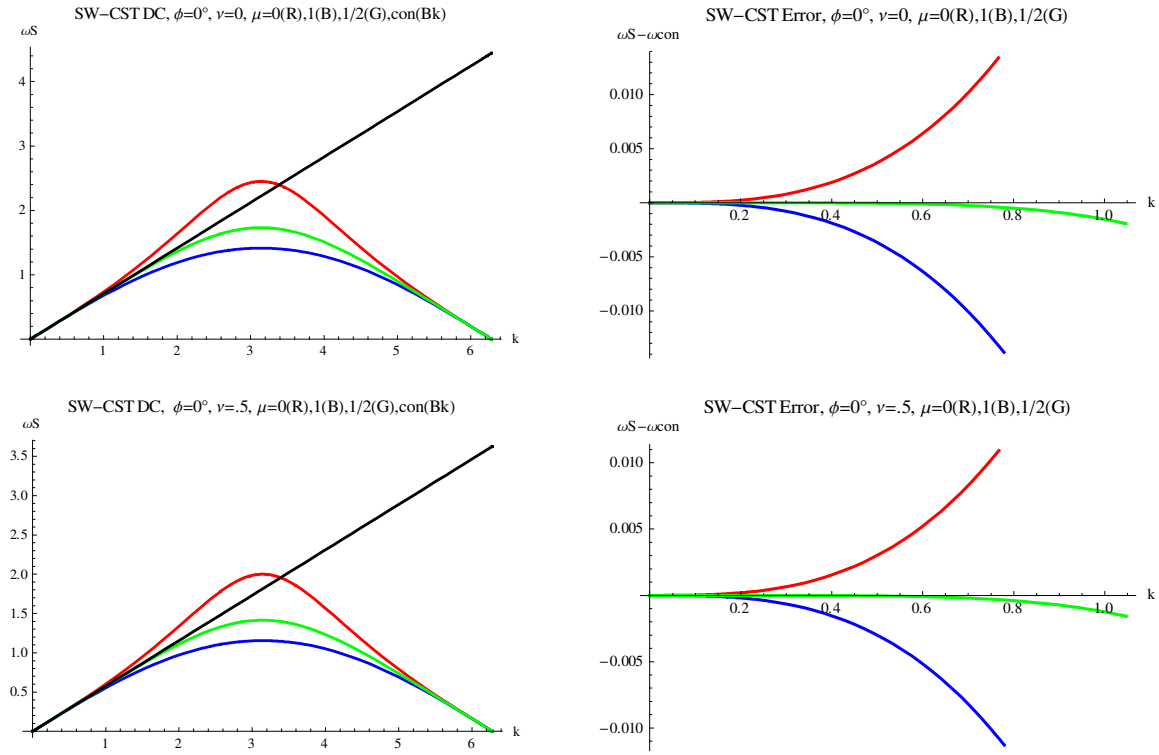

Figure 20. Dispersion curves for S-wave in CST element ($\phi = 0^{\circ}$),CMM (R), DLMM(B), BLFMM(G), continuum (Bk)

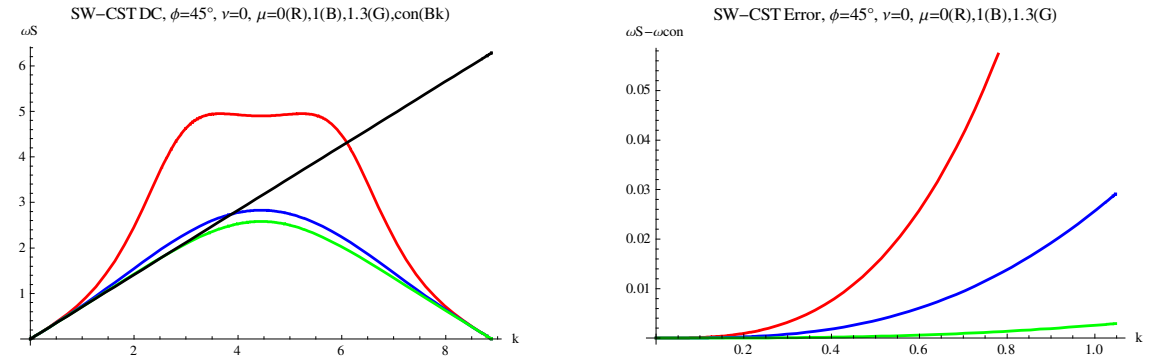

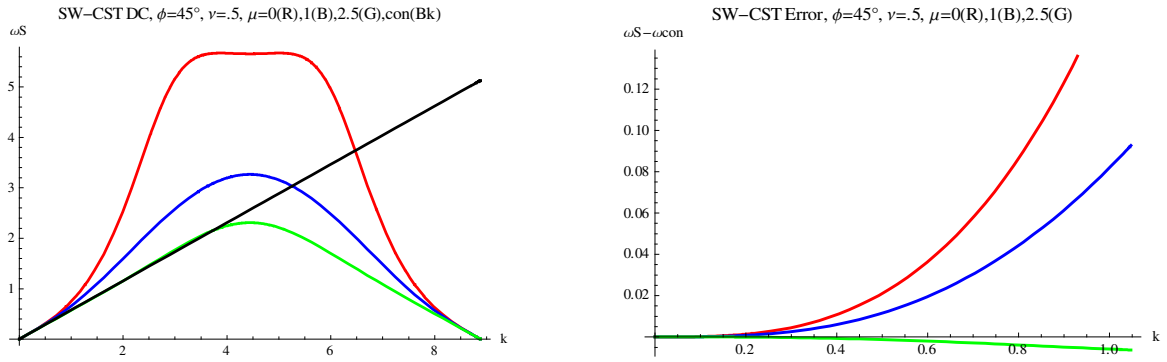

Figure 21. Dispersion curves for S-wave in CST element ($\phi = 45^{\circ}$), CMM (R), DLMM(B), BLFMM(G), continuum (Bk)

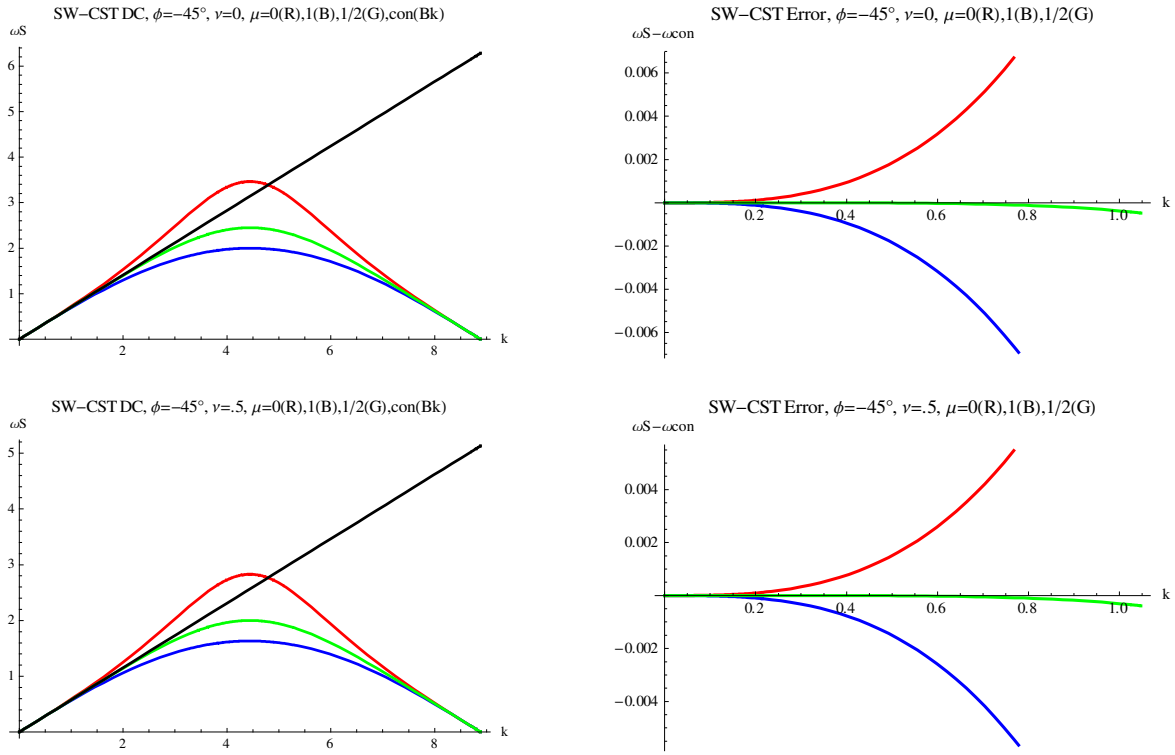

Figure 22. Dispersion curves for S-wave in CST element ($\phi = -45^{\circ}$), CMM (R), DLMM(B), BLFMM(G), continuum (Bk)

4.3 Linear Strain Triangle Element

This section presents results obtained for the LST element.

4.3.1 Best μ by Taylor Expansion

Similarly with the CST element, the μ_{opt} for LST element for P-wave propagation is shown in Figure 23, for S-wave is shown in Figure 24. The average μ_{opt} over $\phi \in [-\pi/2, \pi/2]$ is shown in Figure 25. The average μ_{opt} for P-wave is around 0.5. For S-wave it is around 0.6~0.8.

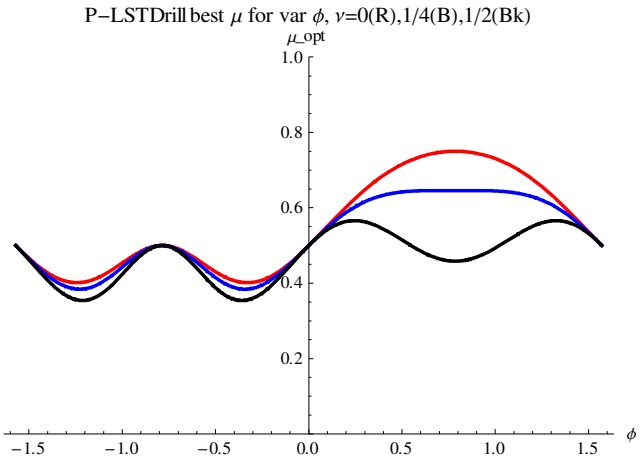

Figure 23. Best u for P-wave, LST element over $\phi \in [-\pi/2, \pi/2]$, v=0(R), 0.25(B), 0.5(Bk)

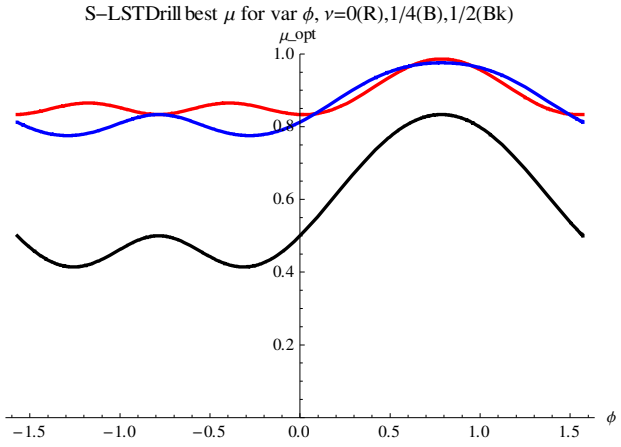

Figure 24. Best u for S-wave, LST element over $\phi \in [-\pi/2, \pi/2]$, v=0(R), 0.25(B), 0.5(Bk)

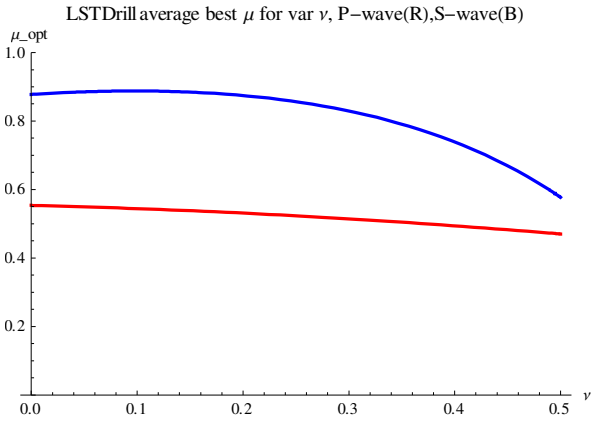

Figure 25. LST average best μ for $\upsilon \in [0,1/2]$, P-wave(R), S-wave(B)

4.3.2 The P-wave for LST-3/9R

The plot of r_{yp} with respect to various ϕ is shown in Figure 26. When $\phi = 0^{\circ}$ and $\phi = 45^{\circ}, r_y = 0$. This means these cases corresponds to the exact plane wave propagation.

The best μ for various rotational angles and Poison ratios can be obtained from Figure 23. We are interested in $\phi = 0^{\circ}, 45^{\circ}, 30^{\circ}$ and $\nu = 0,\ 0.5$. The value of best μ is shown in Table 5.

Table 5. Best μ for P-wave in LST for various ϕ and ν

μ_{opt} ϕ / υ	0°	45°	30°
0	0.5	0.75	0.7
0.5	0.5	0.45	0.5

The FEM dispersion curves comparison with the continuum are shown in Figure 27-29. The same conclusion can be made that the error for the BLFMM is greatly reduced. The CMM and DLMM show larger errors in different directions.

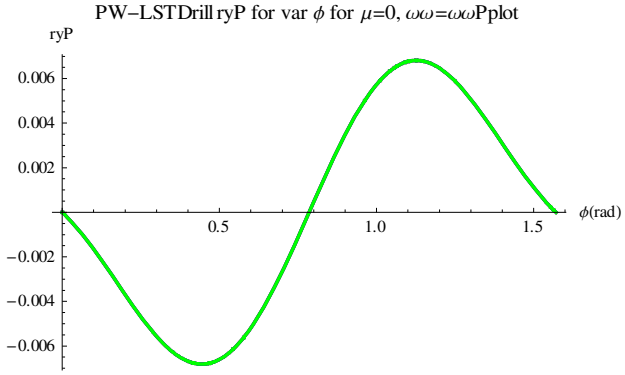

Figure 26. Residual in y axis with various ϕ for P-wave in LST element.

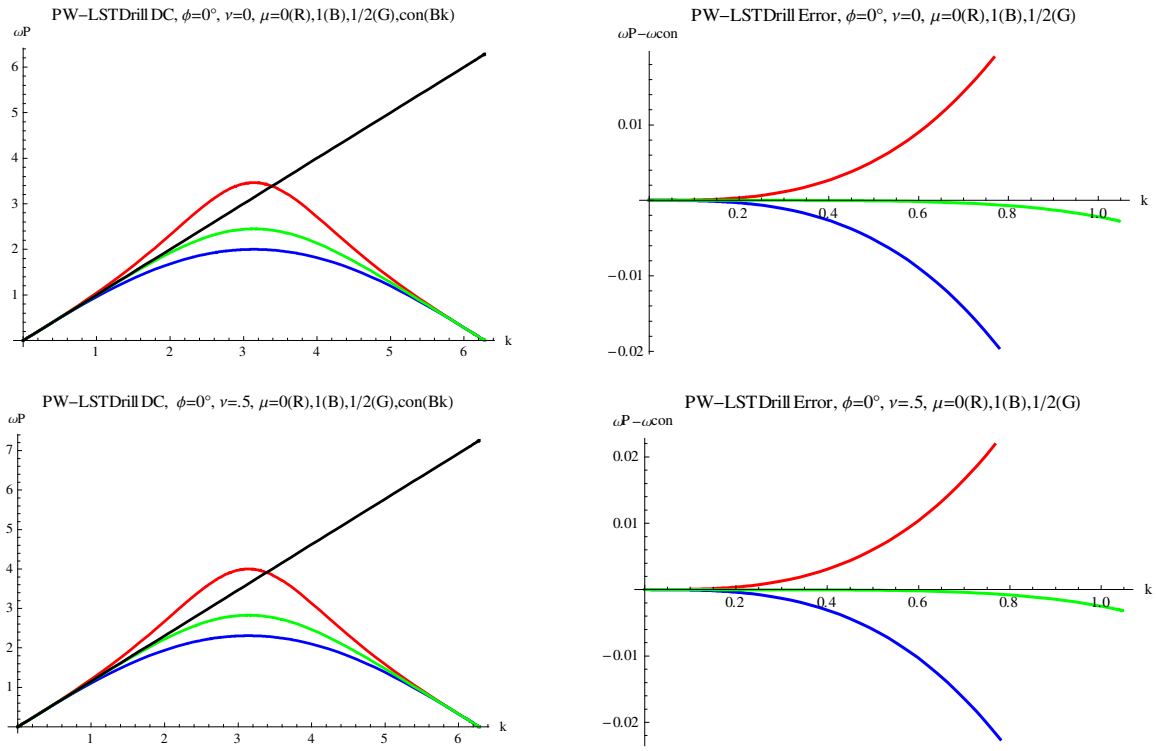

Figure 27. Dispersion curves for P-wave in LST element ($\phi = 0^{\circ}$), CMM (R), DLMM(B), BLFMM(G), continuum (Bk)

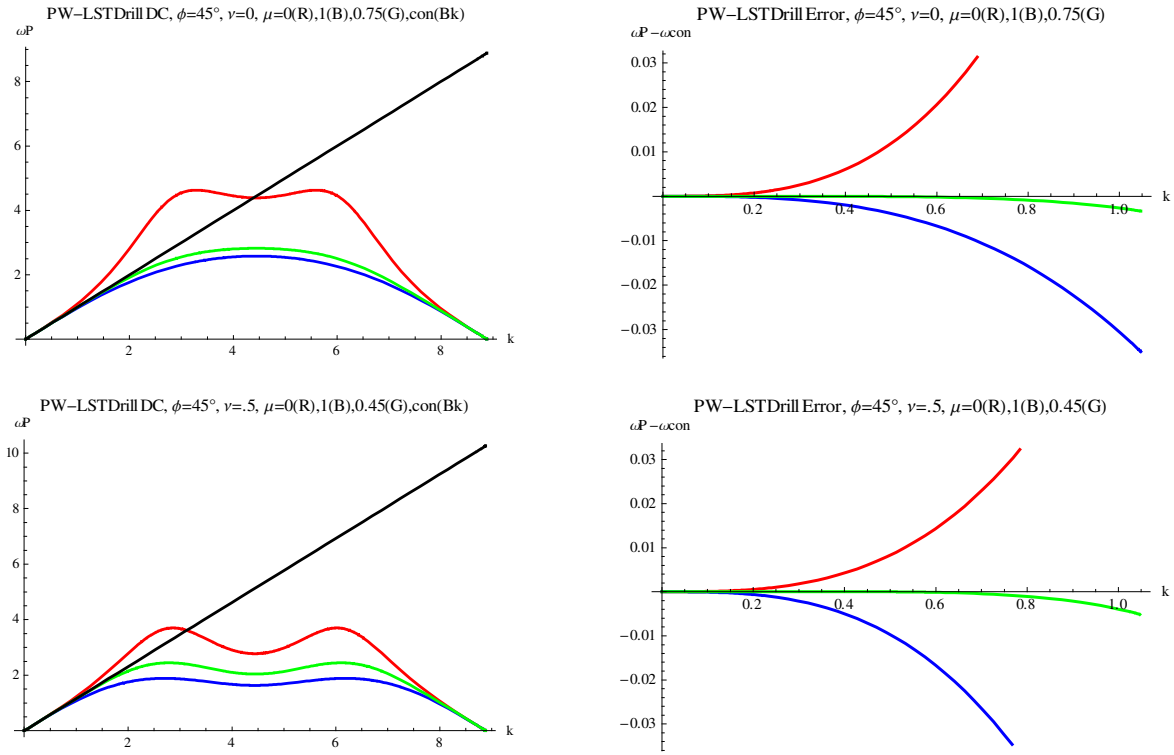

Figure 28. Dispersion curves for P-wave in LST element ($\phi = 45^{\circ}$), CMM (R), DLMM(B), BLFMM(G), continuum (Bk)

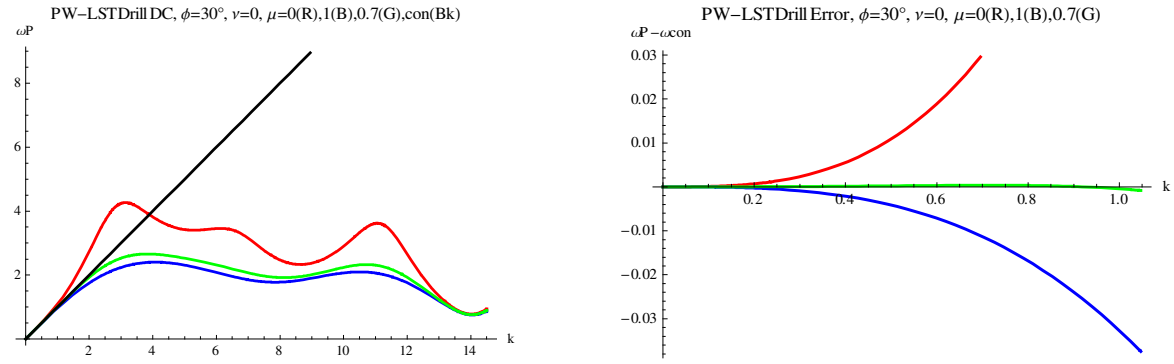

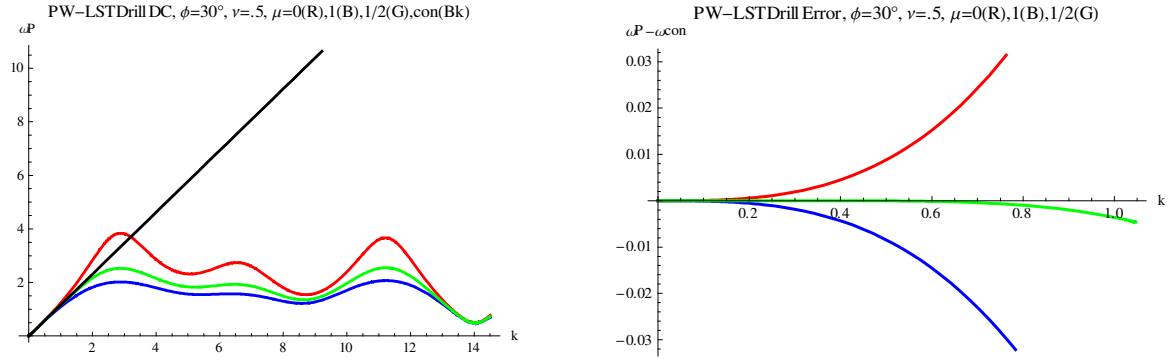

Figure 29. Dispersion curves for P-wave in LST element ($\phi = 30^{\circ}$), CMM (R), DLMM(B), BLFMM(G), continuum (Bk)

4.3.3 The S-wave for LST-3/9R

The plot of r_{xS} with respect to various ϕ is shown in Figure 30. When $\phi = 0^{\circ}$ and $\phi = 45^{\circ}, r_x = 0$. This means these cases corresponds to the exact plane wave propagation. The best μ for various rotational angles and Poison ratios can be obtained from Figure 24. We are interested in $\phi = 0^{\circ}, 45^{\circ}, -45^{\circ}$ and $\nu = 0,\ 0.5$. The values of best μ are shown in Table 6.

Table 6. Best μ for S-wave in LST for various ϕ and ν

μ_{opt} ϕ / υ	0°	45°	-45°
0	0.8	1	0.8
0.5	0.5	0.8	0.5

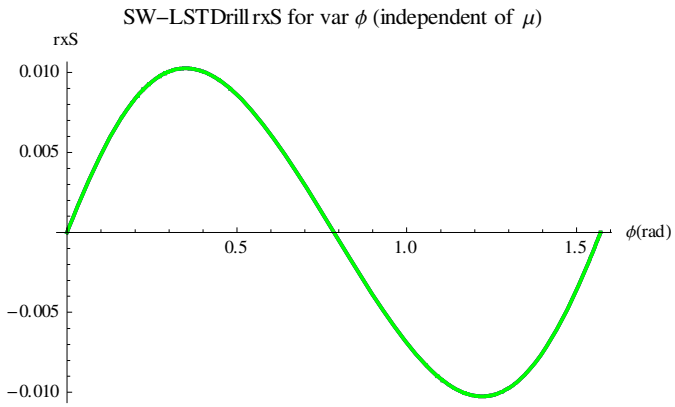

Figure 30. Residual in x axis with various ϕ for S-wave in LST element.

The FEM dispersion curves comparison with the continuum are shown in Figure 31-33. The nonsymmetry of the dispersion curves is caused by introducing the drilling DOFs compared with that of CST element. The same conclusion can be made that the error for the BLFMM is almost zero everywhere. The CMM and DLMM show larger errors in different directions.

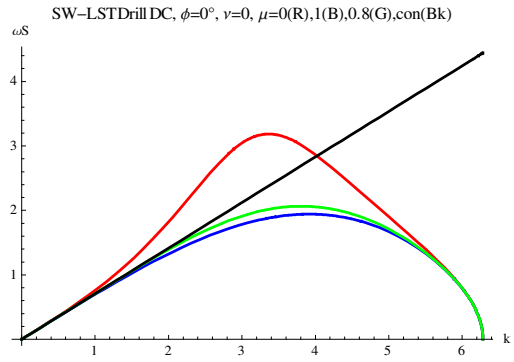

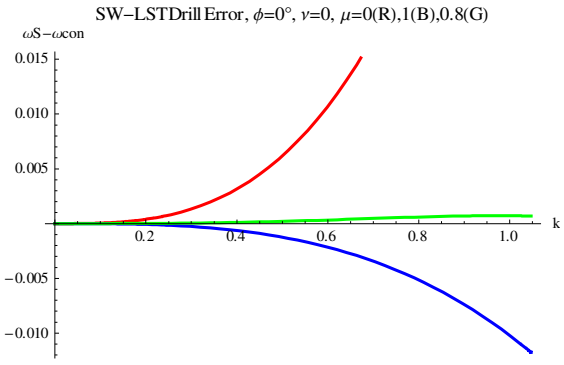

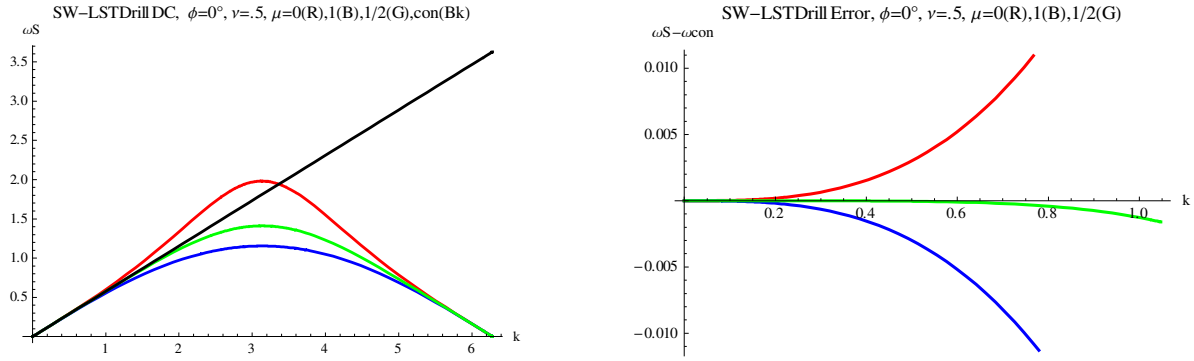

Figure 31. Dispersion curves for S-wave in LST element ($\phi = 0^{\circ}$), CMM (R), DLMM(B), BLFMM(G), continuum (Bk)

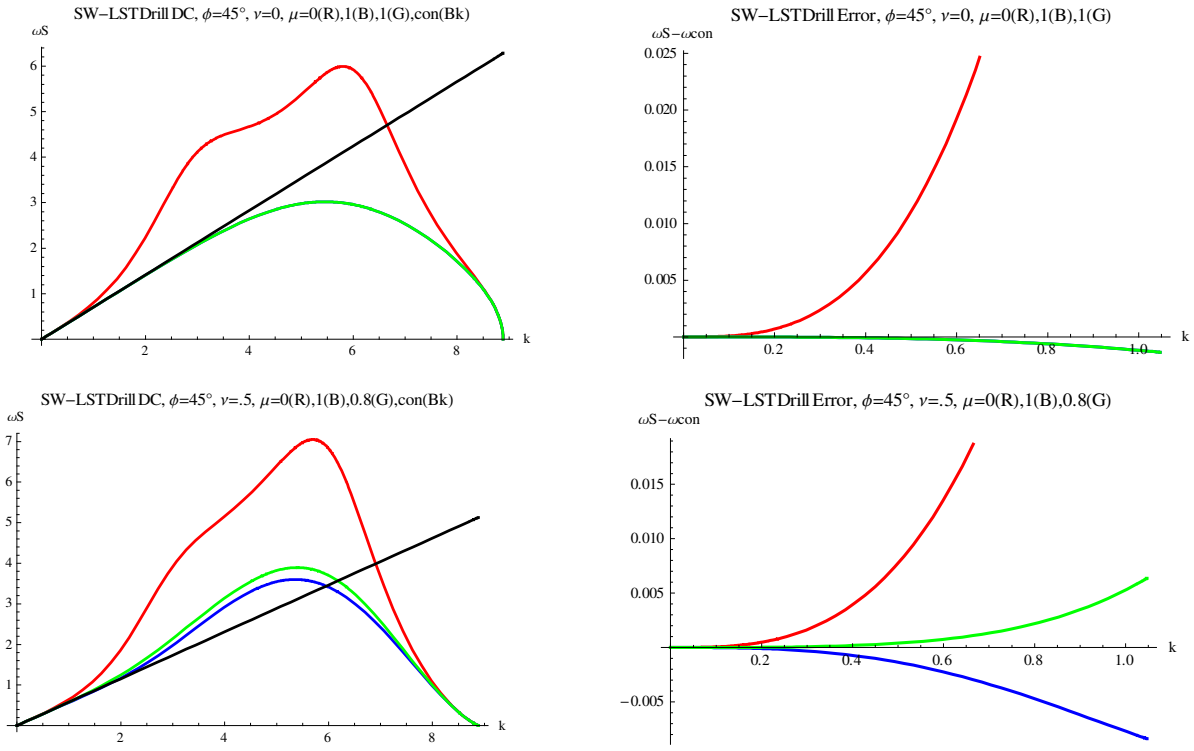

Figure 32. Dispersion curves for S-wave in LST element ($\phi = 45^{\circ}$), CMM (R), DLMM(B), BLFMM(G), continuum (Bk)

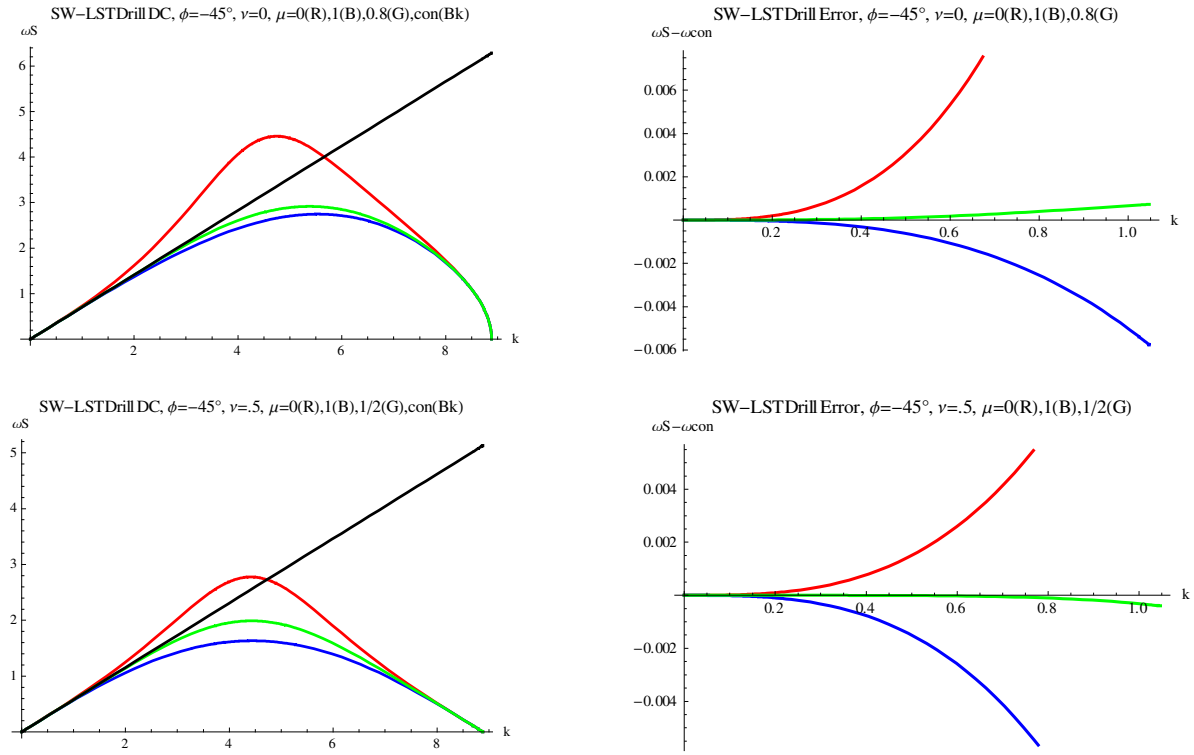

Figure 33. Dispersion curves for S-wave in LST element ($\phi = -45^{\circ}$), CMM (R), DLMM(B), BLFMM(G), continuum (Bk)

4.4 Discussion of Results

From the results for CST and LST element shown in this chapter, several conclusions can be reached. The best mass matrix combination parameter μ depends on Poisson's ratio ν and finite element mesh rotational angle ϕ, for both P-wave and S-wave propagations. The average μ_{opt} for the P-wave swept through CST/LST element is around 0.5. For the S-wave the average μ_{opt} is around 0.75. For several specific cases displayed in the previous figures, the BLFMM shows the best agreement of dispersion curves with continuum in the low frequency (long wavelength) limit. On the other hand, the use of the conventional mass matrix forms shows reduced accuracy. While the DLMM typically underestimate the

continuum frequency, the QCMM typically overestimates it. Consequently the optimal μ usually lies in the [0, 1] range. It should be noted that use of this optimal mass matrix does not increase the computational cost since the element DOF configuration is unchanged.

CHAPTER 5

CONCLUSION AND FUTURE RESEARCH

5.1 Summary of Thesis Work

While mass templates have been systematically studied for one-dimensional bar and beam elements, the present work represents the first study extending such work to two dimensional elements. Such investigations are significantly more involved because of the following features that emerge in multiple dimensions.

- **Plane Wave Types**. While in one dimension only one plane wave type (longitudinal or P-wave) need to be considered, in two dimensions one is faced with two: P-waves (pressure, primary, longitudinal) and S-wave (shear, secondary, transverse). The dispersion behaviors of the two types differ. In three dimensions one would need to consider one P-wave and two S-waves.
- **Lattice Directionality**. A regular infinite FEM lattice can only propagate exact plane waves along certain preferred directions. For a regular lattice built of square isotropic cells, such as those considered in this study, only 4 directions of the propagation angle range $[-\pi/2, \pi/2]$ qualify. For other directions, the plane wave is distorted. This dependence significantly complicates the derivations of dispersion curves.

- **Material Property Effects**. Even restricting consideration to isotropic material, it is found that Poisson's ratio affects the determination of optimal mass matrices, adding one more parameter to consider. In one-dimensional bar and beam elements, such effect disappears.
- **Computational Effort**. Even for simple one dimensional element such as the 2-node bar, the analytical derivation of dispersion curves is significantly helped by the use of computer algebra systems (CAS). For complicated 1D elements (for example, the Timoshenko beam), it becomes an absolute necessity. Use of CAS for simple two-dimensional elements is slowly becoming feasible on desktop and laptop computers because of huge improvements in CPU speed and RAM storage, as well as steady technical improvement in commercial products such as *Mathematica* (the CAS used in this study). Even so, getting timely results for the present work was only feasible by the systematic use of special programming techniques. The use of CAS for complicated 2D elements as well as any type of 3D element is still out of the question.

Some of these difficulties were overcome by restricting optimality studies to the low-frequency (long wavelength, small wavenumber) limit, which is of primary interest in structural dynamics. While directionality and material property effects persist, the dispersion series become a simple polynomial in the wavenumber k and solutions are easy to extract. The determination of such power series, however, would be unwieldy by hand; but it becomes routine using a CAS.

Because of time limitations, the study focused only on two triangular plane-stress elements, both of which are extensively used in research and production FEM codes as membrane component of thin shell elements.

The first part of the thesis focused on the construction of non-diagonal mass matrices using a strain integration approach to produce displacement shape function. For the conventional 3-node and 6-node membrane triangles, this approach was able to produce the well-known consistent mass matrix (CMM) for such elements. When tried on the LST-3/9R triangle, for which CMM was unknown, it produced very complicated results that were felt to have required significant time and effort to disentangle.

This mishap promoted the derivation of the quasi-consistent mass matrix (QCMM) using a basic and higher order decomposition approach very similar to that used for the construction of the ANDES stiffness template. Once the QCMM was derived, a one-parameter mass template was made possible by linearly combing it with its well-known diagonally lumped mass matrix (DLMM). For comparison sake, a similar one-parameter template was tested for the CST membrane element. While in this case both the CMM and DLMM forms are well known, its weighted combination has never been previously investigated.

5.2 Summary of Results

Detailed analysis of the investigation of the one-parameter templates for the two membrane element configurations were presented in Chapter 4. From this study the following conclusions were reached.

(1) The optimal low-frequency mass matrix for these one-parameter templates depend on three factors: Poisson's ratio ν, wave directionality defined by the orientation angle ϕ and plane wave type (P or S).

(2) Factor dependence may be reduced by taking appropriate averages over either the orientation angle ϕ, Poisson's ratio ν, or both. The dependence on wave type (P or S) was kept.

(3) The optimal combination weight μ_{opt} averaged over both ϕ and ν was fairly close to 0.5 for P-wave propagation for both element types. For the S-wave, the average is about 0.75 for both elements. These easy-to-remember values can be recommended to program implementers for cases where ϕ and ν are difficult to ascertain in advance.

(4) In structural dynamic applications where the S-wave is likely to dominate the response, (for example, transverse vibrations of a beam-like structure discretized with LST-3/9R elements), the value $\mu_{opt} = 0.75$ is recommended.

(5) Among the CMM, DLMM, and BLFMM, The BLFMM formed with μ_{opt} agrees best with the continuum in low frequency range. For the high frequency range, they don't match because finer finite element mesh is needed to capture the phenomenon. So the results of high frequency range should not be trusted in FEM.

(6) The nonsymmetry of dispersion curves is caused by adding additional rotational freedoms, compared the results between the CST and LST elements.

(7) Plane wave propagation is distorted in finite element, the discretization changes its nature, called numerical pollution in FEM. Only when the mesh

orientation angles $\phi = 0^{\circ}, 45^{\circ}, 90^{\circ}$, wave propagate as an exact plane wave. Compared to continuum case, every propagation direction is preferred.

5.3 Future Work

The present investigation may be considered a first step in the systematic investigation of mass templates for 2D structural elements. Certain drastic simplifications and restrictions had to be made to get timely results. These are enumerated next.

- Template with one free parameter
- Square-cell lattice of regular mesh pattern
- Isotropic material
- Plane waves that propagate as such
- Only one residual equilibrium equation forced to vanish

These can be selectively relaxed in future studies according to perceived importance. For example the dependence of μ_{opt} on Poisson's ratio ν is rather mild compared to the influence of mesh directionality on S-wave. This suggests that the first extension should be to a template with multiple free parameters, to investigate whether mesh directionality effects can be mitigated. In turn this would require the derivation of parameterized diagonal and non-diagonal matrix forms. The latter would extend the QCMM derived in this research while the former would include parameterized rotational lumped masses associated with drilling DOF. To support such more ambitious studies, computer algebra program may have to incorporate and achieve significant improvements in performance.

REFERENCES

[1] C.A.Felippa, C.M., *Developments in variational methods for high performance plate and shell elments*, in *The American Society of Mechanical Engineers*, T.B. A.K.Noor, J.C.Simo, Editor. 1989: New York. p. 191-216.

[2] MacNeal, R.H., *The evolution of lower order plate and shell elements in MSC/NASTRAN*, in *Finite Element Methods for Plate and Shell Structures*, E. Hinton, Editor. 1986, Pineridge Press: Swansea, UK. p. 85-127.

[3] Felippa, C.A., *A study of optimal membrane triangles with drilling freedoms.* Computer Methods in Applied Mechanics and Engineering, 2003. **192**(16-18): p. 2125-2168.

[4] K. Alvin, H.M.d.l.F., B. Haugen, C. A. Felippa, *Membrane triangles with corner drilling freedoms. I: The EFF element.* Finite Element Anal. Des., 1992. **12**: p. 163-187.

[5] Bergan, P.G. and C.A. Felippa, *A Triangular Membrane Element with Rotational Degrees of Freedom.* Computer Methods in Applied Mechanics and Engineering, 1985. **50**(1): p. 25-69.

[6] Allman, D.J., *A Compatible Triangular Element Including Vertex Rotations for Plane Elasticity Analysis.* Computers & Structures, 1984. **19**(1-2): p. 1-8.

[7] D.J.Allman, *A Compatible Triangular Element Including Vertex Rotations for Plane Elasticity Analysis.* International Journal of Numerical Methods in Engineering, 1988. **26**: p. 2645-2655.

[8] Frey, F., *Shell finite elements with six degrees of freedom per node*, in *American Society of Mechanical Engineers*, T.B.a.J.C.S. A. K. Noor, Editor. 1989: New York. p. 291-316.

[9] Nygard, M.K., *The free formulation for nonlinear finite elements with applications to shells*, in *Div. of Structural Mechanics*. 1986, Norwegian Institute of Technology: Trondheim, Norway.

[10] Bergan, P.G. and M.K. Nygard, *Finite-Elements with Increased Freedom in Choosing Shape Functions.* International Journal for Numerical Methods in Engineering, 1984. **20**(4): p. 643-663.

[11] Carr, A.J., *A refined finite element analysis of thin shell structures including dynamic loadings*, in *Department of Civil Engineering*. 1968, University of California at Berkeley: Berkeley, CA.

[12] Felippa, C.A., *Refined finite element analysis of linear and nonlinear two-dimensional structures*, in *Department of Civil Engineering*. 1966, University of California at Berkeley: Berkeley, CA.

[13] Hartz, J.L.T.a.B., *High order finite element for plane stress.* Journal of the Engineering Mechanics Division, 1967. **93**(EM4): p. 149-174.

[14] Felippa, C.A., *Parametrized Multifield Variational-Principles in Elasticity .1. Mixed Functionals.* Communications in Applied Numerical Methods, 1989. **5**(2): p. 79-88.

[15] Felippa, C.A., *Parametrized Multifield Variational-Principles in Elasticity .2. Hybrid Functionals and the Free Formulation.* Communications in Applied Numerical Methods, 1989. **5**(2): p. 89-98.

[16] Felippa, C.A. and C. Militello, *Variational Formulation of High-Performance Finite-Elements - Parametrized Variational-Principles.* Computers & Structures, 1990. **36**(1): p. 1-11.

[17] K. Alvin, H.M.d.l.F., B. Haugen, C. A. Felippa, *Membrane triangles with corner drilling freedoms. II: The ANDES element.* Finite Element Anal. Des., 1992. **12**: p. 189-201.

[18] K. Alvin, H.M.d.l.F., B. Haugen, C. A. Felippa, *Membrane triangles with corner drilling freedoms. III: Implementation and Performance Evaluation.* Finite Element Anal. Des., 1992. **12**: p. 203-235.

[19] Felippa, C.A., B. Haugen, and C. Militello, *From the Individual Element Test to Finite-Element Templates - Evolution of the Patch Test.* International Journal for Numerical Methods in Engineering, 1995. **38**(2): p. 199-229.

[20] Felippa, C.A. *Recent advances in finite element templates*. in *ECT 2000 Conference*. 2000. Leuven, Belgium: Saxe-Coburn Publications.

[21] Haugen, B., *Buckling and stability problems for thin shell structures using high-performance finite elements*, in *Dept. of Aerospace Engineering Sciences*. 1994, University of Colorado Boulder: Boulder, CO.

[22] Archer, G.C., *A technique for the reduction of dynamic degrees of freedom.* Earthquake Engineering & Structural Dynamics, 2001. **30**(1): p. 127-145.

[23] Chung, J.T. and G.M. Hulbert, *A Family of Single-Step Houbolt Time Integration Algorithms for Structural Dynamics.* Computer Methods in Applied Mechanics and Engineering, 1994. **118**(1-2): p. 1-11.

[24] Kujawski, J. and R.H. Gallagher, *A Generalized Least-Squares Family of Algorithms for Transient Dynamic Analysis.* Earthquake Engineering & Structural Dynamics, 1989. **18**(4): p. 539-550.

[25] Belytschko, T. and W.L. Mindle, *Flexural Wave-Propagation Behavior of Lumped Mass Approximations.* Computers & Structures, 1980. **12**(6): p. 805-812.

[26] Hughes, T.J.R., ed. *Analysis of transient algorithms with particular reference to stability behavior*. Computational Methods for Transient Analysis. Vol. 1. 1983, Elsevier Science: New York. 68-155.

[27] O.C. Zienkiewicz, R.L.T., *The Finite Element Method*. 4th ed. 1989, London: McGraw-Hill Book Company.

[28] Hinton E., R.T.a.Z., O C, *A note on mass lumping and related processes in the finite element method.* Earthquake Engrg. Struct. Dynamics, 1976. **4**: p. 245-249.

[29] Cook, R.D., Malkus, D.S. and Plesha, M.E., *Concepts and applications of the Finite Element Analysis*. 3rd ed. 1989: Wiley.

[30] Malkus, D.S.a.P., M. E., *Zero and Negative Masses in Finite Element Vibration and Transient Analysis.* Comp. Meths. Appl. Mech. Engrg., 1986(59): p. 281-306.

[31] Malkus, D.S. and M.E. Plesha, *Zero and Negative Masses in Finite-Element Vibration and Transient Analysis.* Computer Methods in Applied Mechanics and Engineering, 1986. **59**(3): p. 281-306.

[32] Malkus, D.S., M.E. Plesha, and M.R. Liu, *Reversed Stability Conditions in Transient Finite-Element Analysis.* Computer Methods in Applied Mechanics and Engineering, 1988. **68**(1): p. 97-114.

[33] I. Fried, D.S.M., *Finite element mass matrix lumping by numerical integration with no convergence rate loss.* Int. J. Solids. Struct., 1975. **11**: p. 461-466.

[34] Archer, G.C. and T.M. Whalen, *Development of rotationally consistent diagonal mass matrices for plate and beam elements.* Computer Methods in Applied Mechanics and Engineering, 2005. **194**(6-8): p. 675-689.

[35] Hauret, P., *Mixed interpretation and extensions of the equivalent mass matrix approach for elastodynamics with contact.* Computer Methods in Applied Mechanics and Engineering, 2010. **199**(45-48): p. 2941-2957.

[36] Khenous, H.B., P. Laborde, and Y. Renard, *Mass redistribution method for finite element contact problems in elastodynamics.* European Journal of Mechanics a-Solids, 2008. **27**(5): p. 918-932.

[37] A. Tkachuk, B.I.W., M. Bischoff. *Discretization of dynamic contact using singular hybrid mass matrices*. in *the 6th European Congress on Computational Methods in Applied Sciences and Engineering* 2012. Vienna, Austria: Vienna University of Technology, Austria.

[38] Felippa, C.A., *Construction of Customized Mass-Stiffness Pairs Using Templates.* Journal of Aerospace Engineering, 2006. **19**: p. 241-258.

[39] Bowles, R.V.a.J.B., *Fourier Analysis of Numerical Approximations of Hyperbolic Equations*. 1982: Socirty for Industrial and Applied Mathematics.

[40] Park, K.C. and D.L. Flaggs, *An Operational Procedure for the Symbolic Analysis of the Finite-Element Method.* Computer Methods in Applied Mechanics and Engineering, 1984. **42**(1): p. 37-46.

[41] Park, K.C. and D.L. Flaggs, *A Fourier analysis of spurious modes and element locking in the finite element method.* Computer Methods in Applied Mechanics and Engineering, 1984. **46**: p. 65-81.

[42] Bergan, P.G., *Finite-Elements Based on Energy Orthogonal Functions.* International Journal for Numerical Methods in Engineering, 1980. **15**(10): p. 1541-1555.

[43] Hanssen, P.G.B.a.L., *A new approach for deriving "good" finite elements*, in *MAFELAP II Conference*, J.R. Whiteman, Editor. 1976, Academic Press: Brunel University. p. 483-498.

[44] Przemieniecki, J.S., *Theory of Matrix Structural Analysis*. 2 ed. 1985, New York: Dover Publications.